Calculations on an electrostatic zoom lens using a charge density method

van Heijst, C.P.M.

Award date:
1988

Eindhoven University of Technology

Department of Physics

Surface Physics Group

Calculations on an electrostatic zoom lens using a charge density method

C.P.M. van Heijst

master's thesis (afstudeerverslag) May 1986

coaching:
ir. H. Ottevanger
prof. dr. H.H. Brongersma

Summary

In ion scattering spectroscopy ions which have been reflected from the surface of a solid are analysed with respect to their energy spectrum. It is of importance that the scattered ions are focused onto the entrance of the energy-analyser. Besides it is necessary that their energy can be adapted to the analyser's pass energy. Using an electrostatic zoom lens the combination variable energy - constant focusing can be realised.
The present zoom lens is of unusual conical symmetry. For calculating the lens properties an available charge density method has been adapted and extended. In this method, a boundary element method, first the charge density distribution at the lens electrodes is calculated. Next particle trajectories can be calculated for arbitrary starting conditions.
Results of trajectory calculations have been used to obtain zoom lens curves. One of the conclusions is that up to pre-accelerations by a factor 6 the scattered ions can be focused in the desired way.

Table of Contents

1. Introduction

1.1 Surface Physics

In surface physics the properties of the outermost atomic layers of a solid are studied. Differences with the underlying bulk layers can be described in terms of e.g. surface segregation and relaxation. The results of surface physics are of critical importance in matters related to adhesion, as with coatings, or related to chemical reactions at a surface, as with catalysis. Further the miniaturising in micro-electronics increases the importance of surface physics.

To study the outermost layers of solids several techniques have been developed. The basic principle of most of them is that a beam of particles or electromagnetic radiation is directed towards a surface. One of the components (ions, electrons, radiation) which is coming back from the surface is analysed with respect to its angle-dependence, energy, frequency or mass. In practice a combination of techniques should be used to get a full understanding of the surface. Examples of well-known techniques are Auger Electron Spectroscopy (AES or Auger), X-ray Photo-electron Spectroscopy (XPS), Low Energy Electron Diffraction (LEED) and Low Energy Ion Scattering (LEIS).

The Auger process is shown schematically in figure 1.1.a. An inner electron shell (of ionisation energy E_A) of some atom is ionised by means of a high-energetic electron or photon. The vacancy created in this way is filled by an outer electron (at energy E_B). The de-excitation energy of this process is used to emit another electron (energy E_F), the so-called Auger-electron. This electron has a kinetic energy characteristic for the emitting atom and is detected.

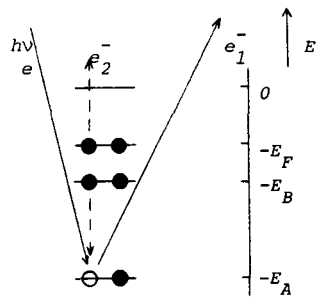

Fig. 1.1.a *Schematic representation of the Auger process*

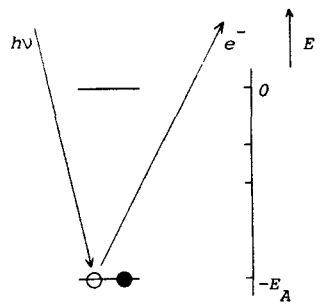

Fig. 1.1.b *Principle of X-ray photo emission*

In figure 1.1.b the principle of the XPS technique, related to AES, has been outlined. Here the ionisation is achieved by an X-ray quantum, and now the energy of the directly ejected electron is object of study. Both AES and XPS inform about the composition of the surfaces. To obtain information about the geometry of a surface LEED can be applied. Here a beam of low energy electrons is directed towards the sample. If the surface layer has a regular structure and if the de Broglie wavelength of the electrons is less than the basic

lengths of the surface primitive cell, electrons can be scattered generating a diffraction pattern. From this the geometry and dimensions of the surface atomic lattice can be calculated by means of the Bragg relation.

The LEIS method, finally, just as Auger and XPS, can be used for element-analysis. The principle and a practical design of an apparatus for this method will be described in next section. It will be shown that LEIS can also be used as a means for structure-analysis.

1.2 Ion scattering, EARISS

In the LEIS technique ions which have been scattered at a surface are detected. In first order approximation the interaction of each ion with the surface can be treated as a classical two particle collision. A classical treatment is allowed because low energy ions, i.e. ions with an energy of several keV's, have a de Broglie wavelength which is negligible in comparison to the effective range of the scattering potential. The collisions are binary because the characteristic distance for perceptible core-core repulsion is far less than the atomic spacings. Further in good approximation the surface atoms are free, for the interaction time of the ions at the surface is short compared to the characteristic time of the lattice vibrations at the surface. Applying the laws of conservation of energy and of momentum a simple expression can be derived, irrespective of the nature of the interaction potential, which relates mass ratio, scattering angle and energy before and after collision. For the special case of an ion (or atom) of mass m_1, being scattered elastically at a heavier target atom (mass m_2) at rest, the energy before and after scattering (E_1 and E_3), the scattering angle θ and the mass ratio $r = m_2/m_1$ are found to be dependent of each other as

$$E_3 = E_1 \left| \frac{\cos\theta + \sqrt{r^2 - \sin^2\theta}}{1+r} \right|^2 . \tag{1.1}$$

So at given E_1, θ and r the energy of the scattered ion can be calculated. (1.1) can be solved towards r, which gives equation (1.2). Equation (1.2) shows the use of ion scattering spectroscopy for element-analysis. For from the experimental parameters uniquely follows the unknown mass-ratio.

$$r = \frac{m_2}{m_1} = \frac{E_1 - 2\sqrt{E_1 E_3}\cos\theta + E_3}{E_1 - E_3} \tag{1.2}$$

LEIS can be made sensitive to the atoms of only one monolayer by scattering noble gas ions. These ions have high neutralisation probability (e.g. 99.9% per collision for He^+ ions) and so ions scattered from deeper layers, which undergo multiple collisions in their way back to the surface, will be neutralised before they can escape from the surface. The surface selectivity attainable in this way is far better than the selectivity of other beam techniques like AES and XPS.

As mentioned before LEIS can also be used for analysis of the surface structure. One source of information is given by the occurrence of double collisions, especially at grazing incidence. The relative number of double collisions depends on the relative positions of the atoms at the surface. Another source of information consists of shadowing effects which are detected if the direction of incidence is such that one type of atoms is hidden behind another type.

At the Surface Physics group of Eindhoven University two experimental setups are available for ion scattering spectroscopy. The first is NODUS (Non-Destructive and Ultra Sensitive single atomic layer surface spectrometer). A schematic diagram of the target section of NODUS is shown in figure 1.2. The energy selection and focusing of scattered ions in this apparatus is

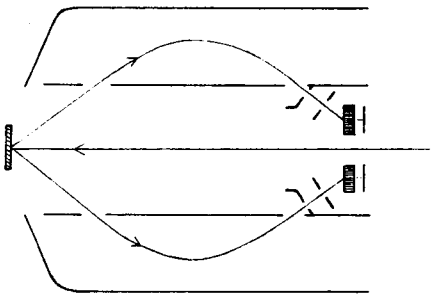

Fig. 1.2 *Cross-section of NODUS*

performed by a so-called cylindrical mirror analyser. For a comprehensive description of NODUS see [Ack-86]. The present report however deals with EARISS, the second apparatus.

A major problem in ion scattering spectroscopy is the surface damage caused by the impact of the ions. The dose of ions can be minimised by maximising the efficiency of detecting scattered ions. To make more efficient use of the scattered ions the past few years a novel apparatus has been built which is capable of imaging at the same time ions scattered at different energies and at different azimuthal angles: the EARISS (Energy and Angle Resolved Ion Scattering Spectrometer). An outline of the apparatus is given in figure 1.3. The primary beam is focused with lens B onto he target. By means of diaphragms D_1 (window) and D_2 (pupil) the (effective) size of the scattering object and the scattering angle are defined. The narrower the diaphragm slits the better defined the angle of scattering but also the lower the intensity of the transmitted secondary beam. In the present design the diaphragms fix the scattering angle at 145 ° with an uncertainty of about 1.5 ° . In future it will be possible to change this scattering angle by means of additional deflection plates in front of the window. Ions which come from the sample with an azimuthal velocity component will have a spiralising path in the analyser before reaching the detector, and so will decrease the (azimuthal) angular resolution. To intercept ions with a too large azimuthal velocity component an azimuth-selector, consisting of several plates with narrow slits, can be placed between D_1 and D_2 [Boe-83]. After passing the pupil the ions are focused by zoom lens E onto the entrance of the analyser. It is this zoom lens which was subject of the present study. It will be dealt with in following sections. In the analyser the ions are spatially separated depending on their energy. Ions of energy E_p , the so-called pass-energy of the analyser, follow the central trajectory shown in figure 1.3, and are focused onto the middle of the detector, whereas ions of higher resp. lower energy are deflected in such a way that finally they are focused onto the detector at smaller resp. larger radial distances. The energy-image at the position of the detector achieved with this analyser is almost linear [Hel-86]. By its shape the analyser furthermore accepts ions in a full azimuthal cone and focuses them onto the detector with an impact angle close to the normal. By the way, strictly speaking beams are not focused onto the the detector itself. In front of the detector there is a couple of channel-plates, at the first of which the focusing occurs. The impact of an ion at the first channel-plate is translated to a gausian shaped cloud of electrons at the detector. The detector, finally, consists of a number of sickle- and ring-shaped conducting electrodes on an isolating plate [Kni-83]. The signals from the electrodes give both the radial and angular position on the

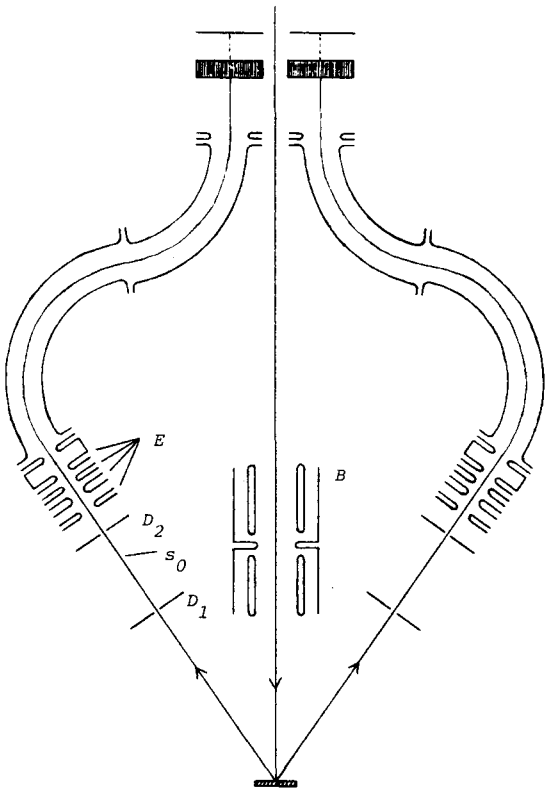

Fig. 1.3 *Cross-section of EARISS*

detector of the electron cloud.

1.3 The zoom lens

When the analyser is operated at a pass-energy E_p ions in the energy-interval $E_p(1-\delta) \leqslant E_p \leqslant E_p(1+\delta)$ can reach the detector. δ is a constant independent of energy, $\delta \approx 1/16$. So when increasing resp. decreasing the pass-energy E_p, larger resp. smaller parts of the secondary spectrum will be detectable. To adapt the ion energy to the pass-energy the ions must be accelerated or decelerated before entering the analyser. Large acceleration must be applied when it is desired to image a considerable part of the secondary spectrum at the same time. Because there is an upper limit to the voltages at which the analyser can be operated, the part which can be imaged at the same time is limited. An alternative to imaging the whole energy in a few parts at the detector is scanning the energy spectrum. If the multidetector is replaced by a single-ring-detector the latter method even is the only possible one. Making an energy scan implies that successively the whole range of energies of the spectrum is accelerated or (for energies higher than E_p) decelerated towards E_p and consequently is imaged at the middle of the detector. An advantage of such a scanning method is that for the successive energies the trajectory in the analyser and the position at the detector is the same. So then the differences in measured intensity cannot be caused by imperfections in the analyser or in the detection system.

During operation the first electrode of the zoom lens is held at target potential. The acceleration or deceleration of the scattered ions from energy E_0 (keV) to energy E_p (keV) at the entrance of the analyser is defined by the potential of the last electrode of the zoom lens, i.e. simply put voltage V_4 (kV) $= -(E_p - E_0)$ to that electrode. The zoom lens however must also be capable of focusing the ions onto the entrance slit of the analyser. This report deals with calculations which have been done to obtain the desired operating of the zoom lens. In chapter 2 the requirements of the lens will be stated precisely and a survey of earlier work (in the design-stage) on the subject will be given. In chapter 3 some methods to calculate lens-properties will be described and the method used here will be explained in detail. Results of (computer-) calculations will be presented in chapter 4. They range from tests on simple lenses for which data by other authors are available to the final model of the EARISS zoom lens. In chapter 5, finally, the results will be discussed and conclusions will be drawn.

2. Characterising the zoom lens

2.1 Ion optics, a description in phase-space

Requirements on charged particle beams in zoom lenses and in other beam transport elements and the properties of such elements can be described in a formalism which is quite analogous to that familiar in light optics. One of the analogies is the resemblance between the index of refraction in light optics and that in ion optics, see figure 2.1.

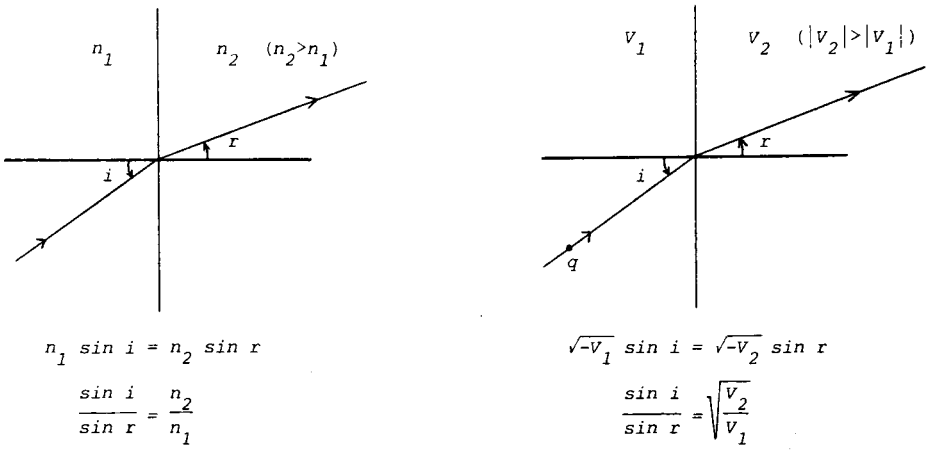

Fig. 2.1 *Refraction in light optics and in particle optics*

Further an electrostatic lens as shown in figure 2.2, which is symmetrical with respect to the z-axis, and which has field-free regions for $z \to \infty$, can be described in terms of focal lengths and principal planes which is identical to the use of these parameters for a cylinder-symmetrical glass lens in light optics. For a definition of these parameters consider the asymptotic behaviour of an ion which comes from the field-free region at the left respectively the right side of the lens, in a direction parallel to the z-axis towards the origin S. The asymptote of the trajectory of the particle after it has passed the region of focusing crosses the z-axis in F_2 and in F_1 and the original asymptote in the principal plane H_2 and H_1 respectively. The distances from H_2 to F_2 and from F_1 to H_1 are denoted by f_2 and f_1 respectively. With the help of F_1, F_2, H_1 and H_2 for each object an image can be constructed in the way shown in figure 2.2 for an object at z_p. For an object at H_1 rigorous continuation of this image-construction method gives an image in H_2. This justifies the construction for an arbitrary trajectory like w in figure 2.2.

A convenient way to calculate trajectories is by means of matrix methods. In first order approximation the displacement r_2 and the angular divergence $r_2' = dr_2/dz$ after each beam transport element can be described as linear transformations of the input parameters r_1 and r_1' at the beginning of the element. So the transformation information can be put in a matrix. The transformation of w in figure 2.2 from z_p to z_q is, in terms of matrix calculation, a multiplication of three matrices:

$$\begin{pmatrix} r_q \\ r_q' \end{pmatrix} = A_3 A_2 A_1 \begin{pmatrix} r_p \\ r_p' \end{pmatrix} = A \begin{pmatrix} r_p \\ r_p' \end{pmatrix}. \tag{2.1}$$

A_1 is the matrix for a transformation in a field-free region (potential V_1) along the distance z_p to H_1. A_2 takes into account the strength of the lens in a transformation from H_1 to H_2, and A_3 again is a matrix for a field-free region (potential V_2), now from H_2 to

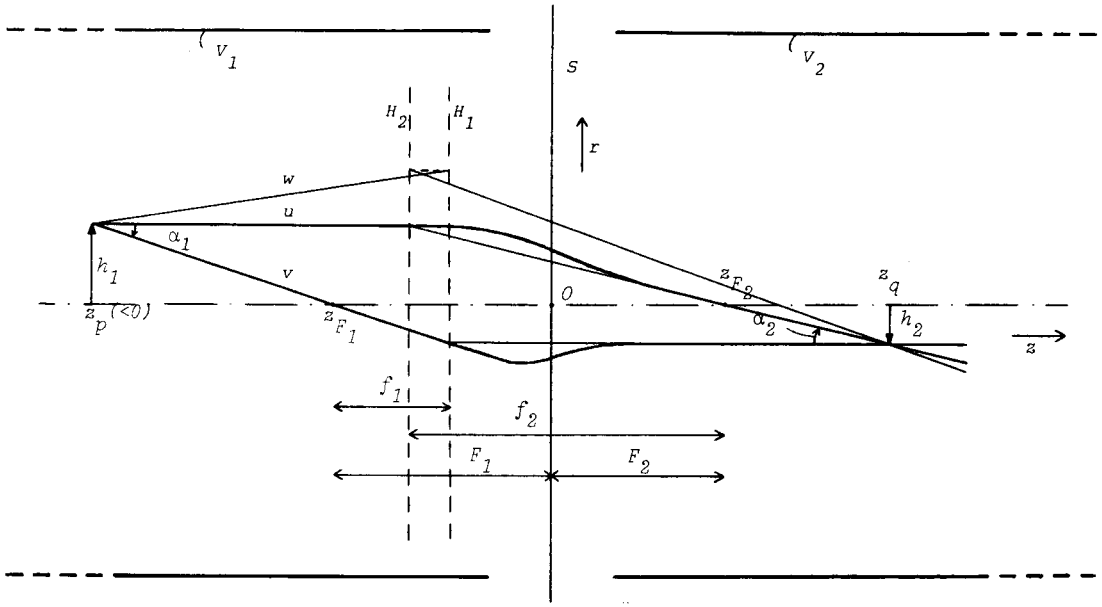

Fig. 2.2 *Image forming in particle optics and definition of focal lengths. f_1, f_2, F_1 and F_2 as shown are positive.*

z_q. The transformation matrices are those well-known from light optics:

$$A_L = \begin{pmatrix} 1 & L \\ 0 & 1 \end{pmatrix} \tag{2.2}$$

for a field-free drift space of length L along the z-axis, and

$$A_f = \begin{pmatrix} 1 & 0 \\ \dfrac{-1}{f_2} & \dfrac{f_1}{f_2} \end{pmatrix} \tag{2.3}$$

for the transformation from H_1 to H_2 in a lens. Multiplication of A_3, A_2 and A_1 gives

$$\begin{pmatrix} r_q \\ r_q' \end{pmatrix} = \begin{pmatrix} 1-\dfrac{z_b-p_2}{f_2} & (p_1-z_v)(1-\dfrac{z_b-p_2}{f_2})+\dfrac{f_1}{f_2}(z_b-p_2) \\ -\dfrac{1}{f_2} & -\left[-\dfrac{f_1}{f_2}+\dfrac{p_1-z_v}{f_2}\right] \end{pmatrix} \begin{pmatrix} r_p \\ r_p' \end{pmatrix}, \tag{2.4}$$

in which

$$p_1 = f_1 - F_1 \tag{2.5}$$

$$p_2 = F_2 - f_2. \tag{2.6}$$

Some further characteristics with respect to figure 2.2 and the matrices can be deduced with the help of the Liouville theorem. This theorem states that for systems the dynamics of which can be derived from a Hamiltonian the flow in the so-called phase-space is incompressible. For a system consisting of particles with no mutual (or negligible) interaction phase-space can be defined to be a six-dimensional space with as co-ordinates the real space co-ordinates (in an orthogonal co-ordinate system) and the conjugate components of momentum. When working in a phase-space based on cylindrical co-ordinates according to Liouville the hypervolume in phase-space containing all $\{r, \phi, z, p_r, p_\phi, p_z\}$ combinations of a beam, measured with respect to the motion of the beam as a whole, will be constant in time. If the motions in the r, ϕ, and z direction, relative to the beam motion, are independent, then the occupied part of phase-space even is restricted to three sections in the (r, p_r), (ϕ, p_ϕ) and (z, p_z) planes, each of which has a constant area. Matrices describing linear transformations in such a plane of constant area have unity determinant [Ban-66]. Applied to the above lens (fig.2.2) this means that a matrix B describing the transformation from (r_p, p_{r_p}) to (r_q, p_{r_q}) has a determinant equal 1. Transformation of co-ordinate (r, p_r) to (r, r') as used in formula (2.1) reveals that matrix A has elements such that

$$det(A) = \frac{\hat{p}_{z_p}}{\hat{p}_{z_q}} det(B) = \frac{\hat{p}_{z_p}}{\hat{p}_{z_q}}. \tag{2.7}$$

in which $\hat{p}_{z_p}$ and $\hat{p}_{z_q}$ denote axial components of momentum, measured with respect to a co-ordinate system at rest (as opposed to p_z, which is relative to the beam motion). In paraxial approximation (2.7) can be put equal to

$$det(A) = \left[\frac{V_1}{V_2}\right]^{1/2}. \tag{2.8}$$

in which V_1 and V_2 denote the potentials at the electrodes measured with respect to the potential at which the kinetic energy of a particle equals zero. From (2.1), (2.2) and (2.3) we obtain

$$det(A) = \frac{f_1}{f_2}. \tag{2.9}$$

and so, combining (2.8) and (2.9),

$$\frac{f_1}{f_2} = \left[\frac{V_1}{V_2}\right]^{1/2}. \tag{2.10}$$

(2.10) is known as the Helmholtz-Lagrange relationship.

The conservation of phase-space area as a consequence of Liouville's theorem as an alternative can be expressed by Abbe's sine law which relates two independent image-forming "rays" like u and v in figure 2.2 as

$$\sqrt{V_1}\, h_1 \sin(\alpha_1) = \sqrt{V_2}\, h_2 \sin(\alpha_2). \tag{2.11}$$

In paraxial approximation (2.11) again reduces to a representation of the Helmholtz-Lagrange relationship:

$$\sqrt{V_1}\, h_1\, \alpha_1 = \sqrt{V_2}\, h_2\, \alpha_2, \tag{2.12}$$

which, with $f_1 = h_2/\alpha_1$ and $f_2 = h_1/\alpha_2$ is equivalent to (2.10). Defining the linear and angular magnification as $M = h_2/h_1$ and $M_\alpha = \alpha_2/\alpha_1$ respectively, (2.12) can be cast into the form

$$M\, M_\alpha = \left[\frac{V_1}{V_2}\right]^{1/2}. \tag{2.13}$$

This relation between M and M_α imposes a severe restriction on the possibilities of a zoom lens.

2.2 The detecting system in terms of phase-space transformations

The zoom lens and other beam transport elements of EARISS will be described in (r,r')-space, with r a local radial distance, measured with respect to the central trajectory s_0 (see figure 1.3). In the following for convenience this space will be denoted as "the" phase-space. The occupied part of phase-space at the pupil is shown in figure 2.3.b. Rays 1 and 2 in this have been drawn in figure 2.3.a.

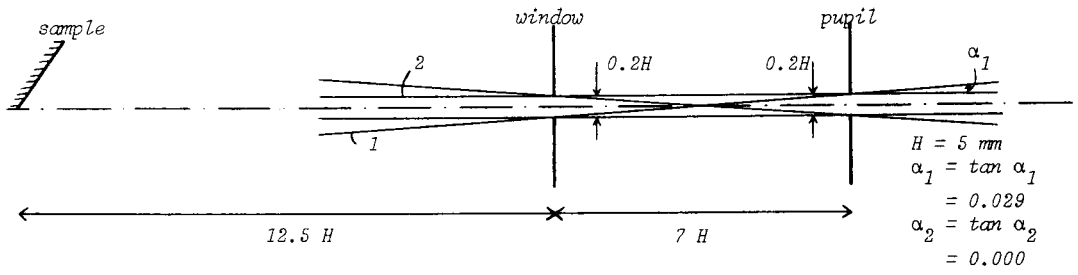

Fig. 2.3.a *The acceptance of particles by the window-pupil combination*

To obtain a maximum energy-resolution within the possibilities of the detector, the phase-plane at the pupil, representing a beam of certain energy, must be transformed to a vertical phase-plane at the position of the detector. The extension in r-direction of this phase-plane must be small. The analyser transforms a vertical phase-plane at its entrance slit (positioned in this case at a distance of 37 mm from the pupil) to an in first order vertical plane at the detector, with a linear magnification of about two [Hel-86]. So the actual focusing must occur in the zoom lens. This can be stated more precisely in terms of optical imaging. See again figure 2.3. The phase-plane at the pupil can be transformed back to the window by tracing back rays 1 and 2, giving a vertical phase-plane at the window. The zoom lens now must image this window-object at the entrance of the analyser, with a minimum linear magnification.

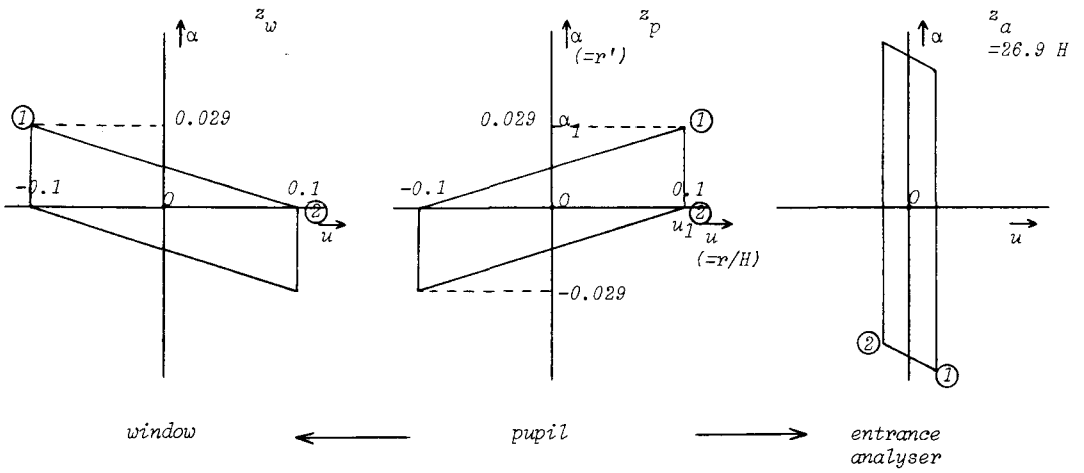

Fig. 2.3.b *Phase-diagram at the pupil, and its transformation back to the window and forward to the analyser entrance*

2.3 Earlier work, design of the zoom lens

The zoom lens was designed using the first order calculations of Boelens [Boe-83]. In his calculations Boelens used as a model for an EARISS zoom lens a slit lens of planar symmetry. Data for such a lens were available in [Har-76]. Some objections can be mentioned against using a lens of planar symmetry as a model for a zoom lens as used in EARISS. It lacks the rotational symmetry and the finite, non-constant radius of curvature of the conical lens in EARISS. New focal lengths must be calculated to characterise such a lens. Before this can be done, however, it must be checked whether the linear transformations introduced in paragraph 2.1 are allowed. Can the lens be considered as symmetrical with respect to the geometrical z-axis (defined in figure 2.5) and, if so, is there linearity in r and r' in first order approximation. Without this a straight z-axis with flat principal planes cannot even be defined.

Generally a lens of fixed position and n elements (on variable potentials $V_1,...,V_n$) can be used to maintain constant $(n-2)$ properties of an image, while the remaining properties are varied. Such a lens has $(n-1)$ independent voltage ratios V_i/V_j, with $i \in (1,...,n)$, and $i \neq j$. When one of these ratios is changed to change a property of the image, the $(n-2)$ remaining can be used to keep constant $(n-2)$ other properties of the image. A restriction is that the Helmholtz-Lagrange relationship (2.13) must be satisfied for each object-image pair. So in the present situation in which the object-image distance must be kept constant while the energy of the image is varied a lens of at least three elements is needed.

The model Boelens used was the three slit lens from [Har-76], with a gap width to slit height ratio of 1.0. The slit height H was taken 4 mm. By means of this lens he made an attempt to image a spectrum from 0 to 4 keV in four parts at the detector while operating the analyser at a pass-energy of 5.5 keV. (In the preliminary design δ for the analyser was 1/11.) With the pupil at a distance of 3 H before the lens (measured with respect to the mid-plane of the lens) and the entrance slit of the analyser 2 H after the lens, only the 0-1 and 1-2 keV sub-spectra could be imaged in the desired way at the analyser entrance. For the 2-3 and 3-4 keV spectra this lens at this position was not appropriate. Particles of these energies, undergoing less acceleration and coupled to this less focusing than those of lower initial energy, were focused at a plane after the analyser entrance.

However by moving the three-element lens a distance H into the direction of the pupil, the image plane could be made to be at the entrance. On account of this observation a four-element lens was proposed which had to be used as a kind of movable three-element lens. This lens is shown schematically in figure 2.4. The data for the voltages to be applied to the lens, and the corresponding co-ordinates of the angular points of the phase plane at the analyser entrance can be found in table 2.1.

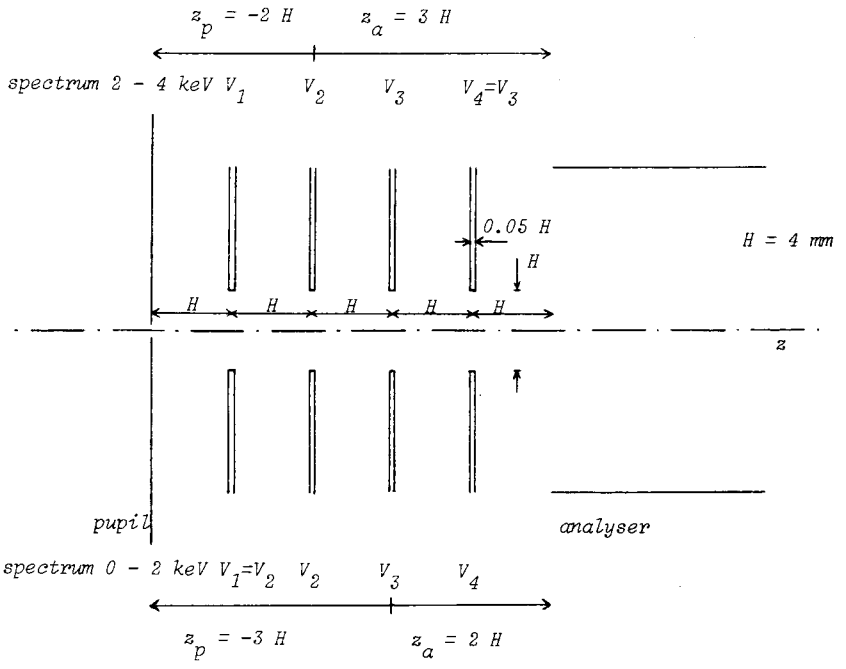

Fig. 2.4 *Schematic cross-section of four slit lens system used in [Boe-83]*

A schematic diagram of the actually constructed lens is contained in figure 2.5.a. Figure 2.5.b shows a representation of this lens which makes it comparable with the lens-system in [Boe-83]. Note that the second aperture has a greater thickness than the other apertures. The intention of this construction-detail is the following: As can be seen from table 2.1 imaging the 3-4 keV spectrum requires (for the model lens in figure 2.4) a voltage of 11 keV on electrode 2. The electrical field strength around this electrode is then in the neighbourhood of 2.75 kV/mm, which is relatively high. To avoid micro-discharges in this situation it is favourable to fit the electrode with relatively smooth edges, i.e. with a large radius of curvature.

Supplementary to the objections mentioned at the beginning of this paragraph, comparison of figure 2.5.b with figure 2.4 gives a further indication to take the data from table 2.1 only as a first start to characterise the zoom lens. In units H e.g. z_p and z_a are considerably larger in figure 2.5.b.

spectrum (keV)	V_1 (kV)	V_2 (kV)	V_3 (kV)	V_4 (kV)	available from [Har-76] $\frac{V_2}{V_1}$	$\frac{V_3}{V_1}$	$\frac{V_4}{V_1}$	phase-plane at the analyser r_1 (mm)	α_1 (rad)	r_2 (mm)	α_2 (rad)
0—1	0	0	-1	-5	1.0	2.0	6.0	0.09	-0.029	-0.14	-0.029
1—2	0	0	-7	-4	1.0	8.0	5.0	-0.17	-0.040	-0.34	-0.039
					1.0	4.5	3.0	0.16	-0.036	-0.17	-0.030
2—3	0	-8	-3	-3	5.0	2.5	2.5	0.13	-0.016	-0.32	-0.033
					3.75	2.0	2.0	0.32	-0.006	-0.18	-0.027
3—4	0	-11	-2	-2	4.75	1.7	1.7	0.19	-0.019	-0.30	-0.030
					3.75	1.4	1.4	0.32	-0.013	-0.17	-0.028

pupil: $r_1 = r_2 = 0.4$ mm $\alpha_1 = 0.026$ rad $\alpha_2 = -0.0087$ rad
$H = 4$ mm

Table 2.1 *Data for imaging a 0-4 keV spectrum in 4 parts at the detector. Calculated using a planar lens model [Boe-83]. Note that V_1, V_2, V_3 and V_4 in $V_2/V_1, V_3/V_1$ and V_4/V_1 are measured with respect to the cathode potential.*

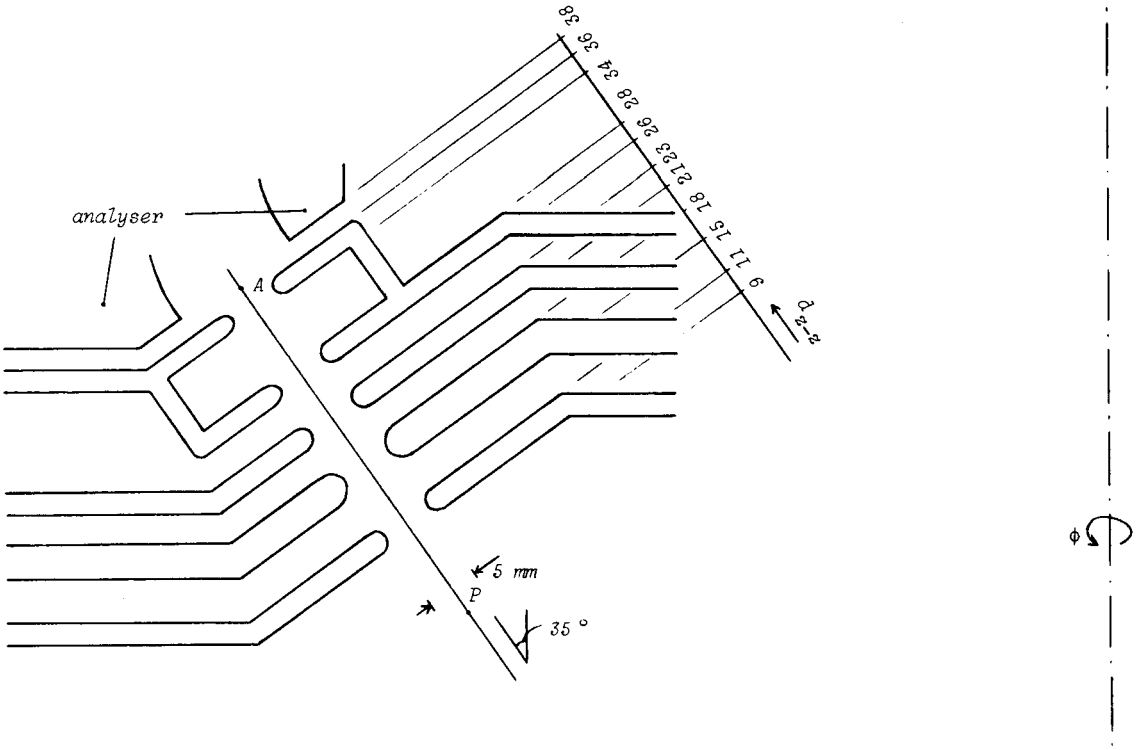

Fig. 2.5.a *Cross-section of EARISS zoom lens, in a meridian plane*

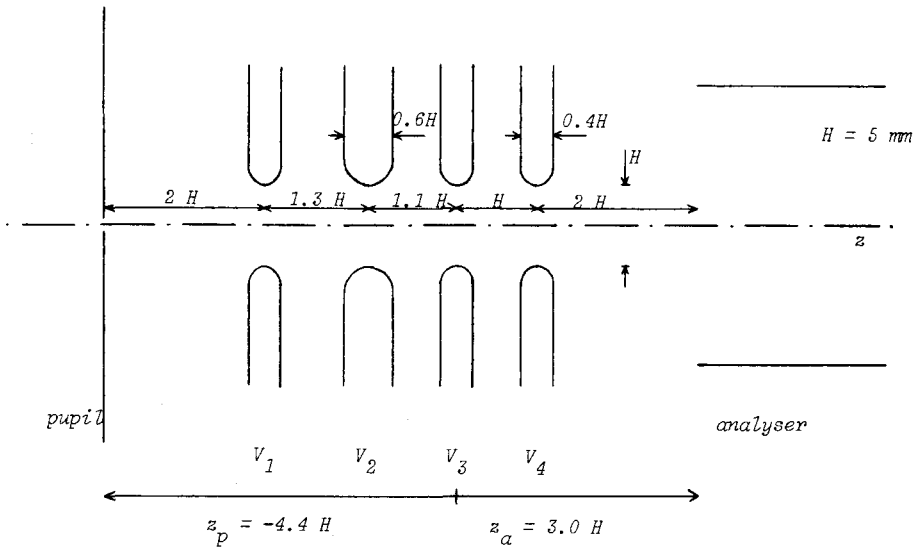

Fig. 2.5.b *Schematic cross-section of EARISS zoom lens, to be compared with figure 2.4*

3. Numerical analysis of particle trajectories

3.1 Methods for field calculation

A review on methods to calculate the properties of electrostatic (and magnetic) lenses of axial and planar symmetry is given by Mulvey and Wallington [Mul-73]. In this report only electrostatic lenses with no space charge inside will be considered. The calculations can almost always be separated into two parts, namely the part concerned with solving Laplace's or Poisson's equation to find the potential distribution within the lens, and that concerned with the ray tracing in order to obtain focal properties. Mulvey and Wallington discuss five computational methods for obtaining the values for the potential. The conformal transformation method, the separation of variables method, the charge density method (c.d.m.), the finite difference method (f.d.m.) and the finite element method (f.e.m.).

In the conformal transformation method the electrode boundaries of an electrostatic lens in a real plane are transformed to a complex plane in which the boundary conditions to be applied to Laplace's equation are simpler. Laplace's equation remains invariant under the transformation. The solution of Laplace's equation in complex space is transformed backwards to real space. In practice the conformal transformation method can only be used to calculate the potential in the plane of symmetry for lenses of planar symmetry.

Characteristic of the technique which is known as the separation of variables method is that the potential is written as a finite series of products of functions in which each function depends on one variable, i.e. co-ordinate, only. The terms of the series are taken to be formal solutions of Laplace's equation with unspecified boundary conditions. As a consequence for example for the case of a cylinder-symmetrical lens the terms usually involve Bessel functions. Unknown coefficients in the series must be determined by applying appropriate boundary conditions.

More generally used than the above two methods are the charge density method, finite difference method and finite element method.

The charge density method has been used in this paper and will be described extensively in next section. Essential for this method is that (in a self-consistent way) the charge density on the electrodes is calculated from the known potential function on the electrodes. The potential function is related to surface charge by an integral equation. In order to solve this equation a point matching method is applied. The electrodes are divided into small parts, and the potential at the centre of each part is calculated. Knowing the charge density at the boundary of the electrodes the potential and electric field at any point inside the lens can be calculated in a straightforward way.

The fourth method mentioned is the finite-difference method. In this method the Laplace operator is, according to the name of the method, approximated by a finite difference. The potential distribution inside a lens can be found by means of a point-matching method. For this purpose the region inside the boundaries of the lens is divided into a mesh and at the mesh lines nodal points are defined. Next the Laplacian at each node is expressed, according to the finite-difference chosen, in terms of the potential at that node and at neighbouring ones. This results in a (band-)matrix equation from which the potentials at the nodes can be solved. The potential and field at non-nodal points can be found with interpolation methods.

A mesh which covers the whole interior of the lens is also used in the finite element method. For N nodal points in this mesh the potential function as a solution of Laplace's equation is expanded in a series of N basis-functions, each of which has the value 1 at exactly one nodal point and 0 at all other nodal points. The expansion coefficients in the series for which the truncation error in the potential is minimal can be found by means of

a variational method. The result is a set of linear equations in the expansion coefficients. Just as in the finite difference method the equations can be combined in a band matrix. A disadvantage of both methods is that, compared to the charge density method, a relatively large computer memory is required to store the elements of the band matrix. An illustration of this can be found in the report of Aarts [Aar-85], who calculated the focal properties of a fairly simple three element lens. A further aspect inherent to the f.d.m. and f.e.m., which is problematic especially when treating lenses with relatively large gaps between electrodes, is that closed boundaries with appropriate conditions on them must be defined. Above-mentioned aspects contributed for a great part to the decision to use the charge density method for calculating the EARISS zoom lens.

3.2 The charge density method

The version of the charge density method which will be treated below is applicable only for electrostatic lenses with rotationally symmetric, metal electrodes. Lenses of conical symmetry like the EARISS zoom lens are special cases of such lenses. Furthermore it is assumed that space charge effects are negligible. The charge density method can also be made applicable to lens systems of other symmetry (or no symmetry at all), lens systems in which dielectrics are included and/or in which space charge effects must be taken into account. When dielectrics are included the appropriate c.d.m. can best be derived from a formal expression of the potential in terms of Green's functions, followed by applying Dirichlet or Neumann boundary conditions to the boundaries of the region of interest. The charge density method is then found to be a special case of the so-called boundary element method (b.e.m.).

The actual c.d.m. is derived directly from the well-known integral form of Poisson's equation:

$$V(\underline{r}) = \frac{1}{4\pi\epsilon_0} \int \frac{\rho(\underline{r}')}{|\underline{r}-\underline{r}'|}\, d^3r'. \tag{3.1}$$

Here $V(\underline{r})$ is the potential at the point $\underline{r}$, ρ is the charge density, and the integration is over all space (occupied by charge). By (3.1) the potential at infinity is implicitly normalised at zero. For systems of cylindrical symmetry it is suitable to use cylinder coordinates (r, ϕ, z) in which the z-axis is the axis of symmetry:

$$V(r,z) = \frac{1}{4\pi\epsilon_0} \iiint \frac{\rho(r',z')}{\sqrt{(r-r')^2+2rr'(1-\cos\phi)+(z-z')^2}} r'dr'dz'd\phi. \tag{3.2}$$

Note that in (3.2) V and ρ because of the symmetry are independent of ϕ. By integration over the azimuth a complete elliptic integral of the first kind $K(k)$ is introduced into the integrand:

$$V(r,z) = \frac{1}{\pi\epsilon_0} \iint \frac{r'K(k)}{\sqrt{(r'+r)^2+(z'-z)^2}} \rho(r',z')dr'dz', \tag{3.3}$$

where

$$K(k) = \int_0^{\pi/2} \frac{d\theta}{\sqrt{1-k^2\cos^2\theta}} \tag{3.4}$$

and

$$k^2 = \frac{4rr'}{(r'+r)^2+(z'-z)^2}. \tag{3.5}$$

With the charge being restricted to the surfaces of the electrodes the integration in r'-z' plane actually consists of line integrals over the electrodes' surfaces. A line integral is most appropriately handled with when switching from the variables z' and r' to the distance s along the line as a new variable. Then z' and r' become functions of s, with $(dr'/ds)^2+(dz'/ds)^2 = 1$, and (3.3) is reduced to

$$V(r,z) = \frac{1}{\pi\epsilon_0}\int \frac{r'\sigma(r',z')K(k)}{\sqrt{(z'-z)^2+(r'+r)^2}}ds', \tag{3.6}$$

where σ is the surface charge density. In the case of two or more electrodes (3.6) must be read as being a formal notation for a set of distinct line integrals.

To calculate the charge density on the surface a point-matching procedure is applied. The intervals of integration are subdivided into N subintervals. In (r,ϕ,z) space this means a subdivision of the electrodes into small rings around the z-axis. The (known) potential at the centre of each subinterval is equated to the sum of the contributions from all subintervals separately:

$$V(r_j,z_j) = \frac{1}{\pi\epsilon_0}\sum_{i=1}^{N}\left| \int_{\text{interval } i} \frac{r\sigma(s)K(k)}{\sqrt{(z-z_j)^2+(r+r_j)^2}}ds \right|. \qquad j=1,\ldots,N \tag{3.7}$$

Next the usual approach (see e.g. [Eng-84]) is to approximate the charge density at each segment i ($i=1$ to N) by an uniform charge density σ_i. From (3.7) then results a set of linear equations from which the σ_i can be solved. In the present report however a different approach is pursued: The charge density is approximated by a smoothed quadratic function. The algorithm which will be described here was developed by Kasper [Kas-83].

The charge density at a segment is expanded into a Taylor series around the midpoint s_i of the segment:

$$\sigma(s) = \sum_{l=0}^{M}\frac{(s-s_i)^l}{l!}\sigma^{(l)}(s_i). \tag{3.8}$$

Further for facility in following derivations the segment width w_i is introduced and the integrand in (3.6) divided by σ is denoted by H:

$$H(s,r_j,z_j) = \frac{rK(k)}{\pi\epsilon_0\sqrt{(z-z_j)^2+(r+r_j)^2}}. \tag{3.9}$$

Substitution of (3.8) and (3.9) in (3.7) gives

$$V(r_j,z_j) = \sum_{l=0}^{M}\sum_{i=1}^{N}\left| \int_{s_i-w_i/2}^{s_i+w_i/2} ds'H(s',r_j,z_j)\frac{(s'-s_i)^l}{l!} \right|\sigma^{(l)}(s_i). \qquad j=1,\ldots,N \tag{3.10}$$

When $\sigma^{(0)}(s_i)$ is separated, and with defining s as a local co-ordinate with respect to the segment's centre, this becomes

$$\sum_{i=1}^{N}\left[\int_{-w_i/2}^{w_i/2} dsH(s_i+s,r_j,z_j)\right]\sigma^{(0)}(s_i) =$$

$$= V(r_j,z_j) - \sum_{l=1}^{M}\sum_{\rho=1}^{N}\left[\int_{-w_\rho/2}^{w_\rho/2} dsH(s_\rho+s,r_\rho,z_\rho)\frac{s^l}{l!}\right]\sigma^{(l)}(s_\rho). \quad j=1,\ldots,N \quad (3.11)$$

In matrix notation the set of equations (3.11) can be replaced schematically by

$$A^{(0)}\underline{\sigma}^{(0)} = \underline{V} - \sum_{l=1}^{M} A^{(l)}\underline{\sigma}^{(l)}. \quad (3.12)$$

As in [Kas-83] M is put equal to 2 and an algorithm is derived for the calculation of $\sigma^{(1)}$ and $\sigma^{(2)}$. $\sigma^{(1)}$ and $\sigma^{(2)}$ are determined in such a way that across the boundaries of segments within an electrode both $\sigma^{(0)}(s)$ and $\sigma^{(1)}(s)$ are continuous. The explanation of the algorithm is based on figure 3.1, where the charge density function on segments n-1 and n of an arbitrary electrode j is shown.

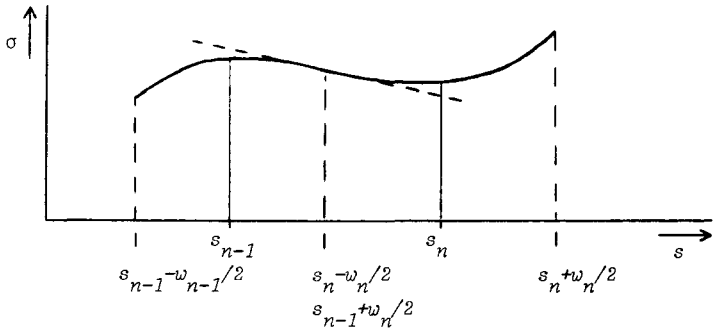

Fig. 3.1 *Charge density function on segments n-1 and n. At* $s = s_n - w_n/2$ *two quadratic parabolas are to be joined together in such a way that they have a common tangent (broken line).*

Electrode j is assumed to have N_j segments in total. The derivatives $\sigma^{(1)}(s)$ at an arbitrary place of the shown interval can be calculated by use of finite difference formula (3.13). This formula is of order two which means that it gives a truncation error equal zero for polynomials of order two or less. Applied at $s = s_n - w_n/2 = \hat{s}_n$, both with forward and backward differentiation based on characteristic s-points, it gives equations (3.14) and (3.15).

$$y'(0) = \frac{3y(0)-4y(-h)+y(-2h)}{2h} \quad (3.13)$$

$$\sigma^{(1)}(\hat{s}_n) = \frac{3\sigma(\hat{s}_n)-4\sigma(s_{n-1})+\sigma(\hat{s}_{n-1})}{2w_{n-1}} \quad (3.14)$$

$$\sigma^{(1)}(\hat{s}_n) = \frac{-3\sigma(\hat{s}_n)+4\sigma(s_n)-\sigma(\hat{s}_{n+1})}{2w_n} \tag{3.15}$$

Combination of (3.14) and (3.15) leads to a tridiagonal system of σ-values at the end-points of the segments $\hat{s}_{n-1}$, $\hat{s}_n$ and $\hat{s}_{n+1}$:

$$k_{n-1}\sigma(\hat{s}_{n-1})+3\left|k_{n-1}+k_n\right|\sigma(\hat{s}_n)+k_n\sigma(\hat{s}_{n+1}) =$$

$$= 4\left|k_{n-1}\sigma(s_{n-1})+k_n\sigma(s_n)\right|, \qquad 2\leqslant n\leqslant N_j-1 \tag{3.16}$$

where

$$k_n = (w_n/2)^{-1}.$$

Because of (3.8) $\sigma(s_{n-1})$ and $\sigma(s_n)$ in (3.16) are equal to $\sigma^{(0)}(s_{n-1})$ and $\sigma^{(0)}(s_n)$ respectively. Applying appropriate boundary conditions for $\sigma(\hat{s}_1)$ and $\sigma(s_{N_j}+w_{N_j}/n)$ the tridiagonal system can be solved to give the charge density at the boundaries of the segments as a function of the charge density at the mid-points of the segments. Which boundary conditions must be applied depends on the geometry of the electrode. If the electrode has a closed end, i.e. $r=0$ for $s=\hat{s}_1$ or $s=\hat{s}_{N+1}$, the first derivatives of σ at that end must be zero. Applying (3.15) and (3.14) for $s=\hat{s}_1$ and $s=\hat{s}_{N+1}$ respectively then results in the equations

$$3\sigma(\hat{s}_1)+\sigma(\hat{s}_2) = 4\sigma^{(0)}(s_1) \tag{3.17}$$

$$\sigma(\hat{s}_N)+3\sigma(\hat{s}_{N+1}) = 4\sigma^{(0)}(s_N). \tag{3.18}$$

If the electrode has an open end a boundary condition can be found from a quadratic extrapolation from the interior values. For $\sigma(\hat{s}_1)$ and $\sigma(\hat{s}_{N+1})$ the equations become

$$k_1\sigma(\hat{s}_1)+(2k_1+k_2)\sigma(\hat{s}_2) = 3k_1\sigma^{(0)}(s_1)+k_2\sigma^{(0)}(s_2) \tag{3.19}$$

$$(2k_N+k_{N-1})\sigma(\hat{s}_N)+k_N\sigma(\hat{s}_{N+1}) = k_{N-1}\sigma^{(0)}(s_{N-1})+3k_N\sigma^{(0)}(s_N). \tag{3.20}$$

The (total) matrix equation which results in the latter case is shown in (3.21).

$$\begin{pmatrix} k_1 & (2k_1+k_2) & 0 & 0 & 0 & 0 & 0 \\ k_1 & 3(k_1+k_2) & k_2 & 0 & & & 0 \\ \cdots & \cdots & \cdots & \cdots & \cdots & \cdots & \cdots \\ 0 & 0 & k_{n-1} & 3(k_{n-1}+k_n) & k_n & 0 & 0 \\ \cdots & \cdots & \cdots & \cdots & \cdots & \cdots & \cdots \\ 0 & & & 0 & k_{N-1} & 3(k_{N-1}+k_N) & k_N \\ 0 & 0 & 0 & 0 & 0 & (2k_N+k_{N-1}) & k_N \end{pmatrix} \cdot \begin{pmatrix} \hat{\sigma}_1 \\ \hat{\sigma}_2 \\ \hat{\sigma}_3 \\ \cdot\cdot \\ \cdot\cdot \\ \hat{\sigma}_{n-1} \\ \hat{\sigma}_n \\ \hat{\sigma}_{n+1} \\ \cdot\cdot \\ \cdot\cdot \\ \hat{\sigma}_{N-1} \\ \hat{\sigma}_N \\ \hat{\sigma}_{N+1} \end{pmatrix} =$$

$$= \begin{pmatrix} 3k_1\sigma^{(0)}(s_1)+k_2\sigma^{(0)}(s_2) \\ 4\left[k_1\sigma^{(0)}(s_1)+k_2\sigma^{(0)}(s_2)\right] \\ \cdots \\ 4\left[k_{n-1}\sigma^{(0)}(s_{n-1})+k_n\sigma^{(0)}(s_n)\right] \\ \cdots \\ 4\left[k_{N-1}\sigma^{(0)}(s_{N-1})+k_N\sigma^{(0)}(s_N)\right] \\ k_{N-1}\sigma^{(0)}(s_{N-1})+3k_N\sigma^{(0)}(s_N) \end{pmatrix}. \tag{3.21}$$

When $\sigma(\hat{s}_1)$ to $\sigma(\hat{s}_N)$ have been obtained the $\sigma^{(i)}$'s needed in (3.11) can easily be calculated:

$$\sigma^{(1)}(s_{n-1}) = 0.5k_{n-1}(\sigma(\hat{s}_n)-\sigma(\hat{s}_{n-1})) \tag{3.22}$$

$$\sigma^{(2)}(s_{n-1}) = k^2{}_{n-1}(\sigma(\hat{s}_n)-2\sigma^{(0)}(s_{n-1})+\sigma(\hat{s}_{n-1})). \tag{3.23}$$

The most straightforward method for solving $\sigma^{(0)}(s_1), \ldots, \sigma^{(0)}(s_N)$ is now the following. With (3.22) and (3.23) $\sigma^{(1)}$ and $\sigma^{(2)}$ in (3.11) can be eliminated. Next the resulting matrix equation can be combined with (3.21) in a novel $(2N+1)\times(2N+1)$ matrix equation in which $\sigma^{(0)}(s_1), \ldots, \sigma^{(0)}(s_N)$, $\sigma(\hat{s}_1), \ldots, \sigma(\hat{s}_{N+1})$ are the unknowns. However for solving this equation by standard methods more than $4N^2$ memory positions are needed. Therefore Kasper proposes to solve (3.11) towards the $\sigma^{(0)}(s_i)$ by means of an iterative solution method, in which the largest parts to store are the three $N\times N$ matrices $A^{(0)}, A^{(1)}$ and $A^{(2)}$.

First of all in this method the matrices $A^{(0)}, A^{(1)}$ and $A^{(2)}$ are calculated by numerical integration on each segment the function $H \cdot s^l/l!$ (see (3.11)). Matrix $A^{(0)}$ is inverted to $A^{(0)-1}$. Secondly a zero order approximation for $\underline{\sigma}^{(0)}$ is calculated from $A^{(0)}\underline{\sigma}^{(0)} = \underline{V}$, or, using the inverse of $A^{(0)}$: $\underline{\sigma}^{(0)} = A^{(0)-1}\underline{V}$. For each electrode separately next the smoothing procedure is applied. This means that first the zero order approximation $\sigma^{(0)}$ is substituted in tridiagonal matrix equation (3.21) (or in a modified matrix equation if the boundary conditions differ) to calculate an approximation for σ at the boundaries of the segments. This σ is, together with the $\sigma^{(0)}$, used to calculate a first approximation for $\sigma^{(1)}$ and $\sigma^{(2)}$ by means of (3.22) and (3.23). After finishing the smoothing procedure the iteration can start: With approximations for $\sigma^{(1)}$ and $\sigma^{(2)}$ the original set of equations (3.11) can be solved to obtain a new approximation for $\sigma^{(0)}$, smoothing is applied, etc. The iteration procedure is made to proceed until (3.24) is fulfilled:

$$\epsilon = \frac{\int_0^{\hat{s}_{N+1}} (\sigma^{(0)[k]}(s)-\sigma^{(0)[k-1]}(s))^2 ds}{\int_0^{\hat{s}_{N+1}} (\sigma^{(0)[0]}(s))^2 ds} \leqslant \epsilon_0, \tag{3.24}$$

where k is the actual iteration number. (3.24) is not the only possible stop-criterion. It must be noted that when using (3.24) locally a great relative error can be admitted.

After calculating the charge density at the electrodes the potential and electric field at any place in space can be calculated from (3.7) and (3.25) and (3.26).

$$E_z = -\frac{\partial V}{\partial z} =$$

$$= -\sum_{i=1}^{N} \int_{segm\ i} ds' \frac{r'(z'-z)}{\pi\epsilon_0[(r'-r)^2+(z'-z)^2][(r'+r)^2+(z'-z)^2]^{1/2}} E(k)\sigma(s') \tag{3.25}$$

$$E_r = -\frac{\partial V}{\partial r} =$$

$$= -\sum_{i=1}^{N} \int_{segm\ i} ds' \frac{r'}{\pi\epsilon_0 r[(r'+r)^2+(z'-z)^2]^{1/2}} \left| \frac{[r'^2-r^2+(z'-z)^2]}{[(r'-r)^2+(z'-z)^2]} E(k) - K(k) \right| \sigma(s') \tag{3.26}$$

Here $E(k)$ is a complete elliptic integral of the second kind.

$$E(k) = \int_0^{\pi/2} \sqrt{1-k^2\sin^2\theta}\, d\theta \tag{3.27}$$

It enters the equations when taking the derivative of K:

$$\frac{dK(k)}{dk} = \frac{1}{k}\left\{ \frac{E(k)}{1-k^2} - K(k) \right\}. \tag{3.28}$$

For calculating focal properties of lenses for a wide range of voltages on the electrodes an equally wide range of calculated charge density distributions must be available. With a lens on which at the same time independently m different voltages $(V_1, V_2, ..., V_m)$ can be set however only m times a charge density distribution needs to be calculated by means of the above procedure. m linearly independent $(V_1, V_2, ..., V_m)$ combinations can by superposition give each desired combination. Superposition in the same way of the corresponding charge density distributions gives the charge density distribution needed.

3.3 Practical aspects

calculation of elliptic integrals

The complete elliptic integrals of first and second kind $K(k)$ and $E(k)$ are calculated using the method of successive Landen's transforms. A subroutine based on this method was developed by Van Engelshoven [Eng-85]. Recurrence relations in three components a, b and c form a scale, from which $K(k)$ and $E(k)$ can be calculated:

$$\begin{cases} a_{n+1} = (a_n + b_n)/2 \\ b_{n+1} = \sqrt{a_n b_n} \\ c_{n+1} = (a_n - b_n)/2 \end{cases} \tag{3.29}$$

$$K(k) = \lim_{n\to\infty} \frac{\pi}{2}\frac{1}{a_n} \tag{3.30}$$

$$E(k) = \lim_{n\to\infty} \frac{\pi}{4a_n}[c_0 - \sum_{i=1}^{n} 2^i c_i^2]. \tag{3.31}$$

The initial values have to be taken as

$$\begin{aligned} a_0 &= 1 \\ b_0 &= \sqrt{1-k^2} \\ c_0 &= 2-k^2. \end{aligned} \tag{3.32}$$

In practice on the average only 3 to 4 iterations have turned out to be necessary for obtaining an accuracy in $K(k)$ and $E(k)$ better than 10^{-10}.

calculation of integrals in general

The matrix elements $A_{ji}^{(l)}$, $j \neq i$, are calculated using a 7-point Gauss rule. The integration subroutine which has been developed is capable of integrating vector functions. $A_{ji}^{(0)}$, $A_{ji}^{(1)}$, $A_{ji}^{(2)}$ are dealt with as being components of a vector function. This saves much overhead time and calculating three times the same elliptic integrals. The accuracy of the integrals which are calculated using above subroutine has been tested by means of integrators based on 15- and 21-point Gauss-Kronrod rules. These integrators were taken from the QUADPACK package ([Pie-83]).

Matrix elements $A_{ii}^{(l)}$ cannot be calculated using the above 7-point formula. When k approaches 1 (see(3.5)), $K(k)$ becomes singular. Actually the singularity is of a logarithmic type. With $\xi^2 = 1-k^2$ it can be derived that

$$\lim_{k\to 1} K(k) = \lim_{\xi\to 0} [\ln\frac{4}{\xi} + \frac{\xi^2}{4}(\ln\frac{4}{\xi} - 1)]. \tag{3.33}$$

One way to deal with an integrand containing such a singularity is to expand the integrand in a series in ξ and next integrate analytically. Another way is to take the logarithmic function $\ln\frac{4}{\xi}$ as a weight function and next derive a special Gauss-type integration formula, just like known formulas like Gauss-Chebyshev can be derived. In present study a 6-point Gauss-type integration formula is used, taken from [Kas-82]. The accuracy of the results when using this formula has been checked by means of a subroutine (QAGS) from QUADPACK which can integrate singularities.

The fields inside a lens are calculated using the same integration subroutines as with the calculation of $A_{ji}^{(l)}$, $j \neq i$. Because the field evaluations are by far the most time consuming part in trajectory calculations an attempt has been made to speed up the integration. When using a Gauss rule with less points probably only about a factor 2 in computer time can be saved without considerable loss of accuracy. A further reduction in time can only be achieved with an automatic integration subroutine which is applied to the whole integration interval of each electrode. Automatic integrators which have been tested in present study are QAGN and QAGS from QUADPACK and AUTINT from ACCULIB (see [Vor-74]), all adaptive routines. They were less economic than was expected. Even with only moderate accuracy requirements they needed more integration points than when successively applying the 7-point formula on all electrode segments. The reason is that the charge density function has a discontinuity in its second derivative at the segments' boundaries, and that the automatic integrators have an error control based on the approximation that higher derivatives in the integrand are smooth. Only an automatic integrator

with a different kind of error control could be efficient in present case.

For positions near the boundaries of the electrodes (3.25) and (3.26) are unsuitable. Special expressions can be derived for this case, see e.g. [Hoo-80]. As an alternative the well-known expression (3.34) for the field at the surface of a conductor, normal to that surface, can be used:

$$E = \frac{\sigma}{\epsilon_0}. \tag{3.34}$$

However because in present study there is no interest in calculating particle trajectories which start from an electrode (i.e. a cathode) or which pass near to an electrode, no attention has been paid to the calculation of near-boundary fields.

matrix solution ($A^{(0)}\sigma^{(0)}=...$)

In previous discussion it was stated that $A^{(0)}\underline{\sigma}^{(0)}=\underline{V}$ and equation (3.12) could be solved using the inverse of matrix $A^{(0)}$. The actual approach however is a bit different. Now the system of linear equations is solved using a so-called Crout-algorithm (see [Vel-81]). In this algorithm matrix A is first decomposed into an upper triangular matrix U and a lower triangular matrix L (: an LU-decomposition). Next $\underline{\sigma}^{(0)}$ is found by solving both of the triangular systems $L\underline{a}=\underline{V}$ (or $\underline{V}$ replaced by the right-hand side of (3.12)) and $U\underline{\sigma}^{(0)}=\underline{a}$. The decomposition of a $(n\times n)$-matrix requires about $n^3/3$ multiplications and divisions (in the following denoted by operations). Solving the two triangular systems takes n^2 operations, which is as much as in a normal matrix vector multiplication $A\underline{x}=\underline{y}$. Calculating the inverse of A is expensive in comparison to an LU-decomposition. It requires at least n^3 operations.

In the original Crout-algorithm a partial pivoting technique was included. However for all lens models which were tested (cylinder lenses, aperture lenses and the EARISS-zoom lens) no interchanges (of rows) in the matrices did actually occur. So in the final version of the algorithm the partial pivoting part was dropped.

Some authors who describe a charge-density method propose to solve the matrix equation using an iterative method like the Gauss-Seidel one or the Jacobi one. Using these methods in present case probably will not be more economic than using a Crout-algorithm. Consider the case of a lens with m independent voltage ratios, where calculation of the charge density distribution takes k^0 steps using Kasper's method. For this lens in total mk^0 times a matrix equation must be solved. All these matrix equations contain the same matrix A. After decomposing A using a Crout-algorithm the solution of the mk^0 matrix equations takes mk^0n^2 further operations. How many operations (in total) are needed when using an iterative matrix solution method cannot be said on beforehand. It depends on the number of iterations. Each step in the iteration (n.b. also the first one) requires n^2 operations (see [Vel-81]). When according to Kasper's method a zero order approximation for $\underline{\sigma}^{(0)}$ has been obtained, this can be taken as first estimation in the iterative solution of the matrix equation for obtaining Kasper's second approximation for $\underline{\sigma}^{(0)}$. And in its turn the second approximation for $\underline{\sigma}^{(0)}$ as first estimation in the calculation of the third approximation for $\underline{\sigma}^{(0)}$, etc. It seems reasonable to assume that using this method in the second to k_0-th step of Kasper's algorithm for each step only a few, say five, iterations will be necessary. So then these steps for m potential combinations will require about $5m(k_0-1)n^2$ operations. The question is, however, how many iterations will be needed to obtain an accurate value of Kasper's zero order approximation for $\underline{\sigma}^{(0)}$. From the above it is clear that only if significantly less than $n/(3m)$ iterations are needed the total costs of an iterative method like Gauss-Seidel or Jacobi can be less than that of a direct method.

matrix solution: tridiagonal matrix

The solution of the tridiagonal system (3.22) is achieved by a subroutine which in fact is a simple version of the Crout algorithm. The matrix is again decomposed, but now only three one-dimensional arrays are needed to store all information about the matrix.

subdivision of the electrodes into segments

Consider an electrode which has a (sharp) corner with opening angle α. It can be proved (see e.g. [Jac-74]) that near that corner the components of electric field vary proportional to $\rho^{(\pi/\alpha)-1}$, where ρ is the distance from the corner. The same proportionality holds for the surface charge density near $\rho=0$. The dependence on ρ is shown for some special cases in figure 3.2.

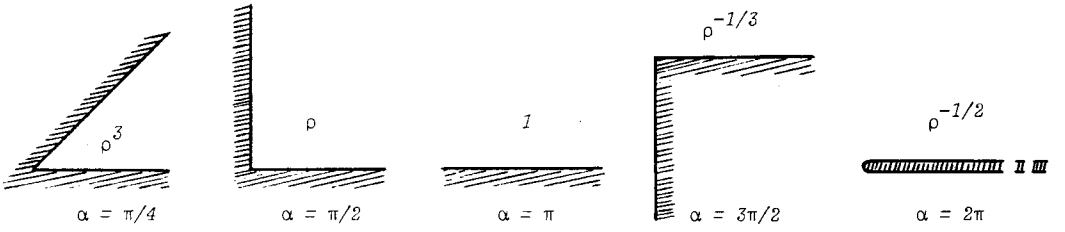

Fig. 3.2 *Variation of the surface charge density (and the components of electric field) with distance ρ from the corner for some opening angles.*

When α is larger than π the charge density becomes singular as $\rho \rightarrow 0$.

An appropriate way to handle this singularity is to choose the widths of successive segments in this area such that the total charge on each segment is the same [Ren-81]. Besides with this method the total number of segments can be kept relatively small (compared to an uniform segment distribution). In the algorithm which has been developed for the segment generation a combination of two types of segment-width distribution are used. The uniform distribution and a distribution ideal for $\alpha=2\pi$ (i.e. the edge of a sheet). In the latter case for the i-th segment from the edge the boundaries and from these the segment width are

$$\begin{aligned} b_{i_1} &= a(i-1)^2 \\ b_{i_2} &= ai^2 \\ w_i &= a(2i-1), \end{aligned} \tag{3.35}$$

where a is the minimal width that is admitted.

3.4 Methods for ray tracing

3.4.1 Straightforward solution of equations of motion

The motion of charged particles in an electric field obeys to

$$m\frac{d^2\underline{r}}{dt^2} = -q\nabla V = q\underline{E}. \tag{3.36}$$

For a system with motion in only two independent directions two components of (3.36) are of interest. Consider motion in x and in z direction in a carthesian co-ordinate system. The pair of equations for this situation can be transferred to four differential equations of first order as shown in (3.37).

$$\begin{cases} \dfrac{dx}{dt} = v_x \\ \dfrac{dv_x}{dt} = \dfrac{q}{m}E_x \\ \dfrac{dz}{dt} = v_z \\ \dfrac{dv_z}{dt} = \dfrac{q}{m}E_z \end{cases} \tag{3.37}$$

Taking time t as independent variable, and for given begin-conditions $\underline{r}(t=0) = \underline{r}_0$ and $\frac{d\underline{r}}{dt}(t=0) = \underline{v}_0$, r and $\frac{d\underline{r}}{dt}$ at any time can be solved by numerical integration of (3.37) using standard methods.

For convenience the above equations have been dealt with in a dimensionless form. With $\underline{r} = L_0\underline{r}^*$, $t = t_0t^*$, and $V = V_0V^*$ (3.36) and the begin conditions become

$$\begin{cases} \dfrac{d^2\underline{r}^*}{dt^{*2}} = -\dfrac{qV_0}{m}\left(\dfrac{t_0}{L_0}\right)^2\nabla^*V^* = \dfrac{qV_0}{m}\left(\dfrac{t_0}{L_0}\right)^2\underline{E}^* \\ \underline{r}^*(t^*=0) = \underline{r}_0\dfrac{1}{L_0} \\ \dfrac{d\underline{r}^*}{dt^*}(t^*=0) = \underline{v}_0\dfrac{t_0}{L_0}. \end{cases} \tag{3.38}$$

Here V_0 is the potential, measured with respect to the place at which the particles have zero kinetic energy. When choosing $|\underline{v}_0| = L_0/t_0$ the factor in front of ∇^*V^* disappears, as can be seen from the law of conservation of energy (3.39).

$$-qV = \frac{1}{2}m\left|\frac{d\underline{r}}{dt}\right|^2 \tag{3.39}$$

Set of equations (3.38) so becomes

$$\begin{cases} \dfrac{d^2\underline{r}^*}{dt^{*2}} = -\dfrac{1}{2}\nabla^*V^* = \dfrac{1}{2}\underline{E}^* \\ \underline{r}^*(t^*=0) = \underline{r}_0\dfrac{1}{L_0} \\ \dfrac{d\underline{r}^*}{dt^*}(t^*=0) = (\cos(\phi_0), \sin(\phi_0))^T, \end{cases} \tag{3.40}$$

in which ϕ_0 is the angle of the particle's path at $t^* = 0$.

3.4.2 Paraxial ray equations

From the equations of motion (3.36) in combination with the energy conservation law (3.39) ray equations can be obtained by elimination of time t. In a carthesian coordinate system (x, y, z) the derivation of a ray equation for x as a function of z proceeds as follows.

With x being a function of z only the x-component of the equations of motion can be written as

$$-\frac{q}{m}\frac{\partial V}{\partial x} = \frac{d^2z}{dt^2}\cdot\frac{dx}{dz} + \left(\frac{dz}{dt}\right)^2\cdot\frac{d^2x}{dz^2}. \tag{3.41}$$

With the help of the z-component of (3.36) d^2z/dt^2 is eliminated. The coefficient $(dz/dt)^2$ must be eliminated using (3.39). For this purpose the latter is put in the form

$$\left(\frac{dz}{dt}\right)^2 = -\frac{2qV}{m}\,\frac{1}{\left(\frac{dx}{dz}\right)^2 + \left(\frac{dy}{dz}\right)^2 + 1}. \tag{3.42}$$

After substitution (3.41) becomes

$$-\frac{q}{m}\frac{\partial V}{\partial x} = \frac{dx}{dz}\left(\frac{-q}{m}\right)\frac{\partial V}{\partial z} + \frac{2\left(\frac{-q}{m}\right)V}{\left(\frac{dx}{dz}\right)^2 + \left(\frac{dy}{dz}\right)^2 + 1}\,\frac{d^2x}{dz^2}. \tag{3.43}$$

An analogous equation is obtained for $y(z)$: simply replace all occurrences of x in (3.43) by y.

Calculating trajectories with a ray equation like (3.43) offers hardly any advantages over the approach of paragraph 3.4.1. Again derivatives of potential V to x and y (and here even V itself), distributed over a two dimensional domain (in (x, z) space) are needed when calculating a set of trajectories. For trajectories near an axis in (x, z) space however paraxial ray equations are derivable in which only the potentials on that axis and its axial derivatives are needed. This will be shown in the following for a system of rotational symmetry and for a system of conical symmetry.

rotation-symmetrical systems

The derivation of a paraxial ray equation for systems of rotational symmetry is well-known from literature. See for example [Gro-81], from which the following derivation was taken. In paraxial approximation x, y, dx/dz and dy/dz are small so higher order terms like $(dx/dz)^2$ and $(dy/dz)^2$ can be neglected. (3.43) now reduces to

$$\frac{\partial V}{\partial x} = \frac{dx}{dz}\frac{\partial V}{\partial z} + 2V\frac{d^2x}{dz^2}. \tag{3.44}$$

Next V around the axis is expanded into powers of x and y; because of symmetry the series is actually one in (x^2+y^2):

$$V(x,y,z) = \Phi(z)+\Phi_1(z)(x^2+y^2)+\Phi_2(x^2+y^2)^2+... \tag{3.45}$$

For $\Phi_1(z)$ and $\Phi_2(z)$ expressions in axial potentials $\Phi(z)$ or derivatives of it can be found from substitution of (3.45) in Laplace's equation $\nabla^2 V=0$. The second order derivatives to x, y and z of V are

$$\frac{\partial^2 V}{\partial x^2} = 2\Phi_1(z) + \Phi_2(12x^2+4y^2) \tag{3.46a}$$

$$\frac{\partial^2 V}{\partial y^2} = 2\Phi_1(z) + \Phi_2(4x^2+12y^2) \tag{3.46b}$$

$$\frac{\partial^2 V}{\partial z^2} = \Phi''(z) + \Phi_1''(z)(x^2+y^2). \tag{3.46c}$$

Next requiring that the coefficients of $(x^2+y^2)^0$ and of $(x^2+y^2)^1$ in Laplace's equation equal zero gives:

$$4\Phi_1(z) = -\Phi''(z) \tag{3.47a}$$

$$16\Phi_2(z) = -\Phi_1''(z). \tag{3.47b}$$

So

$$V(x,y,z) = \Phi(z)-\frac{1}{4}\Phi''(z)(x^2+y^2)+\frac{1}{64}\Phi^{(4)}(z)(x^2+y^2)^2+... \tag{3.48}$$

and in first order approximation we obtain for $V(x,y,z)$, $\frac{\partial V}{\partial x}$ and $\frac{\partial V}{\partial z}$:

$$V(x,y,z) \doteq \Phi(z) \tag{3.49}$$

$$\frac{\partial V}{\partial x} \doteq -\frac{1}{2}\Phi''(z)x \tag{3.50}$$

$$\frac{\partial V}{\partial z} \doteq \Phi'(z). \tag{3.51}$$

Substitution of (3.49), (3.50) and (3.51) in (3.44), with x replaced by r, leads to

$$4\Phi r'' +2\Phi' r' +\Phi'' r = 0. \tag{3.52}$$

If now the potential and its first and second order derivatives to z on the axis are known, from (3.52) paths can be calculated at arbitrary starting conditions for (r,r') at $z=z_0$.

systems of conical symmetry

Also for systems with this symmetry in a straightforward way a paraxial ray equation can be developed. An appropriate co-ordinate system for describing paths around an

axis $\theta=\theta_0$ is the (z',r,ϕ) system from figure (3.3).

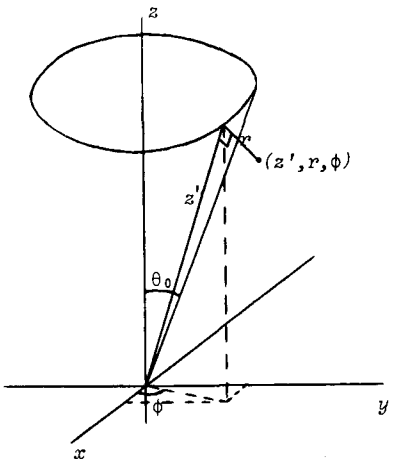

Fig. 3.3 *Local co-ordinate system around* $\theta=\theta_0$

The carthesian co-ordinates (x,y,z) are related to these local co-ordinates as:

$$\begin{cases} x = (bz'+ar)\cos\phi \\ y = (bz'+ar)\sin\phi \\ z = (az'-br), \end{cases} \tag{3.53}$$

where

$$\begin{aligned} a &= \cos\theta_0 \\ b &= \sin\theta_0. \end{aligned} \tag{3.54}$$

The Lagrangian $\tilde{L}(z',r,\phi)$ for an electrostatic system of this symmetry is

$$\tilde{L} = \frac{1}{2}m(\dot{z}'^2+\dot{r}^2+(bz'+ar)^2\dot{\phi}^2) - qV(z',r,\phi). \tag{3.55}$$

This can be checked by transforming the Lagrangian in carthesian co-ordinates $L(x,y,z)$ with the help of (3.53). When $\tilde{L}$ has been obtained, the equations of motion are given by the Eulerian equations:

$$\frac{d}{dt}\frac{\partial\tilde{L}}{\partial\dot{z}'} = \frac{\partial\tilde{L}}{\partial z'} \tag{3.56a}$$

$$\frac{d}{dt}\frac{\partial\tilde{L}}{\partial\dot{r}} = \frac{\partial\tilde{L}}{\partial r} \tag{3.56b}$$

$$\frac{d}{dt}\frac{\partial\tilde{L}}{\partial\dot{\phi}} = \frac{\partial\tilde{L}}{\partial\phi}. \tag{3.56c}$$

For facility of notation from now on z' will be denoted by z. Substitution of (3.55) in the Eulerian equations leads to

$$\ddot{z} = (bz+ar)b\dot{\phi}^2 - \frac{q}{m}\frac{\partial V}{\partial z} \tag{3.57}$$

$$\ddot{r} = (bz+ar)a\dot{\phi}^2 - \frac{q}{m}\frac{\partial V}{\partial r} \tag{3.58}$$

$$z(bz+ar)(b\dot{z}+a\dot{r})\dot{\phi}+(bz+ar)^2\ddot{\phi} = -\frac{q}{m}\frac{\partial V}{\partial \phi}. \tag{3.59}$$

For the derivation of a path equation r is considered as being a function of z. In a way quite analogous to that used in former section t is eliminated. The equation from which is started is now (3.58), and the law of conservation of energy must be written down in (z, r, ϕ) co-ordinates:

$$-\frac{2q}{m}V = \left(\frac{dz}{dt}\right)^2 + \left(\frac{dr}{dt}\right)^2 + (bz+ar)^2\left(\frac{d\phi}{dt}\right)^2. \tag{3.60}$$

The path equation which results is:

$$\frac{2V}{1+\left(\frac{dr}{dz}\right)^2+(bz+ar)^2\left(\frac{d\phi}{dz}\right)^2}\frac{d^2r}{dz^2}$$

$$+\left[\frac{2(bz+ar)bV\left(\frac{d\phi}{dz}\right)^2}{1+\left(\frac{dr}{dz}\right)^2+(bz+ar)^2\left(\frac{d\phi}{dz}\right)^2}+\frac{\partial V}{\partial z}\right]\frac{dr}{dz}$$

$$-\frac{2(bz+ar)aV\left(\frac{d\phi}{dz}\right)^2}{1+\left(\frac{dr}{dz}\right)^2+(bz+ar)^2\left(\frac{d\phi}{dz}\right)^2}-\frac{\partial V}{\partial r} = 0. \tag{3.61}$$

For calculating the focal properties of the EARISS zoom lens only paths with $d\phi/dz = 0$ are taken into account. With $d\phi/dz = 0$ (3.61) reduces to

$$\frac{2V}{1+\left(\frac{dr}{dz}\right)^2}\frac{d^2r}{dz^2}+\frac{\partial V}{\partial z}\frac{dr}{dz}-\frac{\partial V}{\partial r} = 0. \tag{3.62}$$

In paraxial approximation a further simplification can be achieved by putting $1+(dr/dz)^2$ equal to 1. By the way the equation is then the same as (3.44). The reason is that in case of $\dot{\phi}=0$ equations (3.57), (3.58) and (3.59) have the same form as the equations of motion in carthesian co-ordinates.

Next V, $\partial V/\partial z$ and $\partial V/\partial r$ must be expressed in the potential Φ on the axis $r=0$ (i.e. $\theta=\theta_0$) or in Φ's derivatives to z. As in the former section for solving this problem V around the axis is expanded into a Taylor series and substituted into Laplace's equation. The Taylor series to be applied here is one in r. Because of symmetry ϕ does not occur in it:

$$V(z,r,\phi) = \Phi(z)+\Phi_1(z)r+\Phi_2(z)r^2+\Phi_3(z)r^3+... \tag{3.63}$$

Laplace's equation in (z,r,ϕ) co-ordinates can be derived from

$$\nabla^2 V = \frac{1}{e_1 e_2 e_3}\left[\frac{\partial}{\partial z}\left(\frac{e_2 e_3}{e_1}\frac{\partial V}{\partial z}\right) + \frac{\partial}{\partial r}\left(\frac{e_1 e_3}{e_2}\frac{\partial V}{\partial r}\right) + \frac{\partial}{\partial \phi}\left(\frac{e_1 e_2}{e_3}\frac{\partial V}{\partial \phi}\right)\right], \tag{3.64}$$

where

$$e_1 = e_2 = 1 \tag{3.65}$$

$$e_3 = (bz+ar). \tag{3.66}$$

So

$$0 = (bz+ar)\nabla^2 V$$

$$= \frac{\partial}{\partial z}((bz+ar)\frac{\partial V}{\partial z}) + \frac{\partial}{\partial r}((bz+ar)\frac{\partial V}{\partial r}) + \frac{1}{(bz+ar)}\frac{\partial^2 V}{\partial \phi^2}. \tag{3.67}$$

Substitution of (3.63) gives for the three terms in (3.67)

$$\frac{\partial}{\partial z}((bz+ar)\frac{\partial V}{\partial z}) =$$

$$= b\Phi'+b\Phi''z+(a\Phi''+b\Phi_1'+b\Phi_1''z)r+(a\Phi_1''+b\Phi_2'z)r^2+... \tag{3.68a}$$

$$\frac{\partial}{\partial r}((bz+ar)\frac{\partial V}{\partial r}) =$$

$$= a\Phi_1+2b\Phi_2 z+(4a\Phi_2+6b\Phi_3 z)r+(...\Phi_3+...\Phi_4)r^2+... \tag{3.68b}$$

$$\frac{1}{(bz+ar)}\frac{\partial^2 V}{\partial \phi^2} = 0. \tag{3.68c}$$

In order to satisfy $\nabla^2 V = 0$ the coefficients of the terms in r^0, r^1, r^2, etc., in $\nabla^2 V$ must be equal zero. From (3.68):

$$\text{coeff } r^0 = 0: \quad (a\Phi_1+2b\Phi_2 z) = -(b\Phi'+b\Phi''z) \tag{3.69.0}$$

$$\text{coeff } r^1 = 0: \quad (4a\Phi_2+6b\Phi_3 z) = -(a\Phi''+b\Phi_1'+b\Phi_1''z) \tag{3.69.1}$$

$$\text{coeff } r^2 = 0: \quad (...\Phi_3+...\Phi_4) = -(a\Phi_1''+b\Phi_2'+b\Phi_2''z) \tag{3.69.2}$$

.

.

$$\text{coeff } r^n = 0: (...\Phi_{n+1}+\cdots\Phi_{n+2}) = -(a\Phi_{n-1}''+b\Phi_n'+b\Phi_n''z). \tag{3.69.n}$$

Equation (3.69.n) gives a solution for Φ_{n+2} if in former equations Φ_{n+1}, Φ_n and Φ_{n-1} (and especially derivatives to z of the latter two) have been calculated. The first equation (3.69.0) however in principle contains the two unknowns Φ_1 and Φ_2. To make a solution possible in present case the choice $\Phi_1 \equiv 0$ has been made. This means (see (3.63)) that in first order approximation the potential has been taken to be symmetric with respect to the $z-$axis (of the local co-ordinate system). Equations (3.69.0), (3.69.1) and following are

now solved successively:

$$\Phi_2 = \frac{-\Phi' - \Phi'' z}{2z} \tag{3.70}$$

$$\Phi_3 = \frac{-a\Phi'' - 4a\Phi_2}{6bz} = \frac{a}{6b}\frac{(2\Phi' + \Phi'' z)}{z^2}, \tag{3.71}$$

etc.

To obtain a paraxial ray equation in terms of Φ only the expression for Φ_2 is needed. In first order approximation V, $\frac{\partial V}{\partial z}$ and $\frac{\partial V}{\partial r}$ in (3.62) are:

$$V \doteq \Phi \tag{3.72a}$$

$$\frac{\partial V}{\partial z} \doteq \Phi' \tag{3.72b}$$

$$\frac{\partial V}{\partial r} \doteq 2r\Phi_2 = -(\Phi' + \Phi'' z)\frac{r}{z}. \tag{3.72c}$$

With (3.72) and for $z \neq 0$ the final paraxial ray equation becomes

$$2\Phi r'' + \Phi' r' + \left(\frac{\Phi'}{z} + \Phi''\right) r = 0. \tag{3.73}$$

It is interesting to compare this paraxial ray equation with that for systems of planar symmetry. The derivation for the planar symmetry case is given amongst others by [Gro-81] and leads to

$$2\Phi x'' + \Phi' x' + \Phi'' x = 0. \tag{3.74}$$

We find that there is only difference between (3.73) and (3.74) when Φ'/z is not small compared to Φ''. For $z \to \infty$, when the radius of curvature in the conical system approaches ∞, there is no difference at all.

3.4.3 Integrating differential equations, practical aspects

In the original version of the program the integration of the differential equations (3.40) was performed using a Runge-Kutta code of order 4 with constant step size. Tests did show that when tracing a trajectory from one side of a two element lens to the other side for only moderate field gradients already 40 steps had to be taken to achieve an acceptable accuracy. Then for each trajectory 160 derivative, i.e. electric field, evaluations are needed. In present case the electric field is very expensive to evaluate. It requires integration over the surfaces of all electrodes, multiple calculation of elliptic integrals, etc. For this reason an attempt has been made to find a code which uses a minimum of derivative evaluations. In accordance with a recommendation in [Hoo-80] first DIFFSYS from [Bul-66] was tested. This code, based on an extrapolation method, however appeared not to be efficient in present case. For situations in which the Runge-Kutta code needed 160 evaluations DIFFSYS took not less than 225 evaluations. Further it did give relatively few output points. Finally a solution has been found in taking code STEP from DEPAC ([Sha-75]). This code, a step oriented integrator, uses a variable order, variable step Adams method. In [Sha-76] this and other codes are extensively compared, and one concludes that it is one of the most efficient codes when equations are very expensive to evaluate. In present case it appears to require less than 100 evaluations where the Runge-Kutta code requires 160. Besides if the accuracy demands are increased the number of function

evaluations increases only moderately. And as another advantage at very low cost extra output points can be obtained using an associate interpolation routine INTRP.

The integration of the paraxial ray equations is also performed using STEP and INTRP. In the calculations the axial potential function has been approximated by a series of coupled polynomials of degree 2 (compare the charge density function on the electrodes' surfaces). Although by doing so a discontinuity of the second derivative is introduced, for moderate accuracy demands no problems did arise when using STEP for the integration.

4. Results

4.1 2-element cylinder lens

Cylinder lenses are frequently used in particle optics because they are simply to align. Besides they screen beams from stray fields. For the idealised case of two coaxial cylinders of half-infinite length held at different potentials but with no gap between them, the potential distribution can be expressed exactly in terms of Bessel functions. But for the case of cylinders separated by a finite distance no exact solution does exist. Further in such lenses the potential distribution, and so the focal properties, depend on the wall-thickness of the cylinders. Several authors present calculated data for cylinder lenses. Most accurate data for thin-walled lenses are believed to be those of Harting and Read [Har-76]. Thick-walled lenses have been described accurately by Natali et al. [Nat-72]. In the following only data for thin-walled cylinder lenses will be calculated. When calculating the charge density on the surfaces of these lenses the charge sheets on the inside and outside surfaces can be regarded as a single charge sheet. So the number of segments needed when using a charge density method is halved.

gap $G = 0.1D$

The smallest gap G : lens diameter D ratio used by Harting and Read is 0.1. For comparison a lens with this G/D value was also dealt with in present study. The lens model used consisted of two cylinders with open ends at $z = -5.0$ and $z = 5.0$ (in units D). Harting and Read closed the ends of the cylinders with a 30 ° cone, for computational reasons as they said. In present lens model the cylinder ends were left opened. The cylinders were divided into 30 segments, with a minimum segment width 0.045 and a maximum width 0.5. Some calculated trajectories, for voltage ratios V_2/V_1 from 5 up to 80, are shown in figure 4.1.

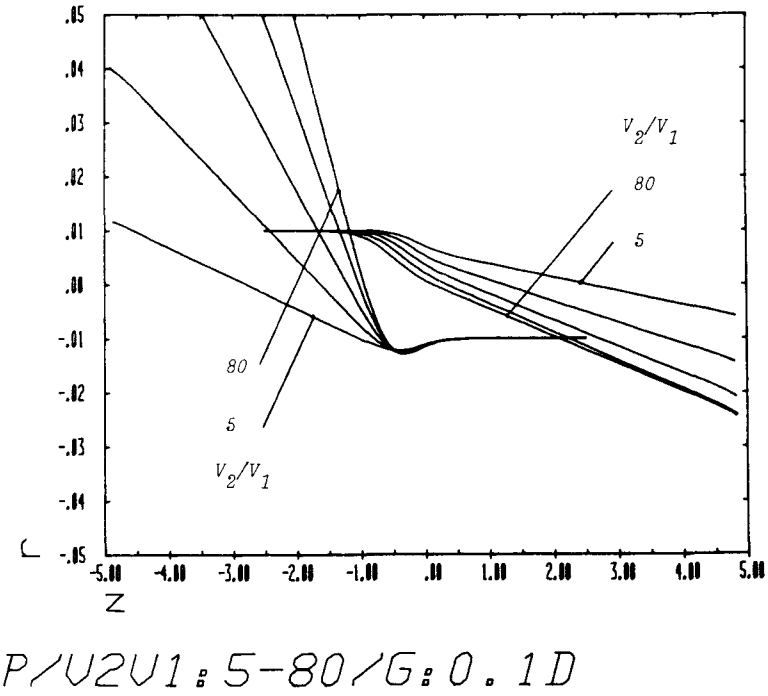

Fig. 4.1 *Particle trajectories for several values of* V_2/V_1. $G = 0.1D$

V_1 and V_2 are the voltages applied to the left and right electrode. They are measured with

respect to that voltage at which the particle's kinetic energy equals zero. The trajectories were obtained from a straightforward integration of the equations of motion as described in section 3.4.1. The integration took about a hundred function evaluations. When calculating the trajectories care must be taken not to start too near the ends of the lens. From tests it appeared that best can be started at a distance greater than about 1.5 D from the end. The focal lengths corresponding to the trajectories of figure 4.1 are given in table 4.1, together with the results of Harting and Read (who give their results in not more digits than shown). As can be seen there is a good agreement.

$\frac{V_2}{V_1}$	present results $N=30$				[Har-76] $N=560$			
	f_1	F_1	f_2	F_2	f_1	F_1	f_2	F_2
5.0	1.76	2.78	3.95	2.48	1.77	2.78	3.95	2.48
10.0	0.80	1.62	2.54	1.18	0.80	1.62	2.54	1.19
20.0	0.45	1.20	2.04	0.64	0.46	1.21	2.05	0.64
40.0	0.30	1.03	1.90	0.32	0.30	1.03	1.90	0.32
80.0	0.22	0.95	1.97	0.10	0.22	0.94	1.97	0.10

Table 4.1 *Focal lengths for lens* $G=0.1D$

A more direct check of the accurateness of the charge density method used is possible by means of a comparison with data provided by Van Hoof [Hoo-80]. Using a charge density method with extrapolation of the results he calculates for a cylinder lens of gap $G=0.1D$ (and with cylinder length $L=5D$) the axial potential function when $(V_1,V_2)=(-1,1)$. In the following this function will be denoted by $\Phi_0(z)$. Van Hoof claims his calculations have an accuracy of about 10^{-5} %.

z/D		0.025	0.1	0.25	0.5	1.0
$\Phi_0(z)$	present results $N=30$	0.06527	0.2554	0.5711	0.8572	0.9864
	present results $N=52$	0.06553	0.2564	0.5728	0.8575	0.9868
	Van Hoof $N=\infty$	0.06559	0.2566	0.5731	0.8577	0.9868

Table 4.2 *Axial potential* $\Phi_0(z)$ *for lens* $G=0.1D$

Results of present calculations, for two values of segment number N, are compared with (rounded) data of Van Hoof in table 4.2. Present data disagree by up to 0.5 % for $N=30$ and by up to 0.1 % for $N=52$. In [Hoo-80] no calculated data are given for the axial potential when $(V_1,V_2)=(1,1)$ ($:\Phi_1(z)$). [Hoo-80] seems to assume, just as [Har-76] does, that in that case the axial potential exactly equals 1 for all z. Results of present calculations ,not shown, for $N=30$ and $N=52$, differ about 0.2 % from that value.

gap $G=1.0D$

In previous work in our group Van Engelshoven [Eng-85] calculated a few focal lengths for a lens with $G=1.0D$ using a simple charge density method. Mainly to check the accuracy of present work in comparison with his work focal properties have been calculated for the $G=1.0D$ case too. The basic lens model used in present study consisted of

two cylinders with open ends at $z=-6.0$ and at $z=6.0$, which were divided into $N=32$ segments of widths between 0.5 and 0.45 (all in units D). The results of Van Engelshoven disagree by 2 up to 3 % with those of Harting and Read. Present results for the same voltage ratios have a much better agreement. See table 4.3.a, $N=32$, and table 4.3.b.

	present results											
	N = 32				N = 56				N = 84 (long lens)			
$\frac{V_2}{V_1}$	f_1	F_1	f_2	F_2	f_1	F_1	f_2	F_2	f_1	F_1	f_2	F_2
5.0	2.64	4.13	5.91	3.72	2.63	4.11	5.89	3.71	2.63	4.13	5.89	3.71
10.0	1.16	2.34	3.66	1.69	1.15	2.32	3.64	1.68	1.15	2.33	3.62	1.67
20.0	0.63	1.69	2.80	0.82	0.63	1.68	2.79	0.82	0.62	1.68	2.78	0.80
40.0	0.39	1.41	2.47	0.33	0.39	1.40	2.47	0.33	0.39	1.41	2.45	0.32
80.0	0.27	1.28	2.43	0.01	0.27	1.28	2.42	0.01	0.27	1.28	2.41	0.00

Table 4.3.a *Focal lengths for lens $G=1.0D$. present results*

	Harting and Read (1976)				V. Engelshoven (1984)
$\frac{V_2}{V_1}$	f_1	F_1	f_2	F_2	F_1
5.0	2.59	4.13	5.79	3.57	4.01
10.0	1.12	2.35	3.55	1.56	2.29
20.0	0.61	1.71	2.71	0.72	---
40.0	0.38	1.44	2.39	0.26	---
80.0	0.26	1.31	2.36	-0.06	---

Table 4.3.b *Focal lengths for lens $G=1.0D$. previous results*

However the overall agreement with [Har-76] is less than that in table 4.1. Using formula (2.10) for checking the results didn't bring relief. Using the f_2 and f_1 values listed in table 4.1 to calculate f_2/f_1 gives results for the new calculated series and that of [Har-76] which have same order of magnitude. The difference with the theoretical $(V_2/V_1)^{\frac{1}{2}}$ is less than 1 % in both series.

It was tried to achieve a better agreement with [Har-76] by using smaller segments ($N=56$) and by besides taking cylinders with their ends at $z=-10.0$ and $z=10.0$ ($N=84$).

The influence of this on the axial potential can be seen from table 4.4, where $\Phi_0(z)$ and $\Phi_1(z)$ have been listed. $\Phi_1(z)$ (for $N=32$) besides has been plotted in figure 4.2. Changing from $N=32$ to $N=56$ gives a maximal change in $\Phi_0(z)$ of 0.7 %. The change in $\Phi_1(z)$ is (relatively) smaller, namely less than or equal to 0.2 %. The further increase of N (to 84) by means of lengthening the cylinders causes only minor differences in $\Phi_0(z)$: up to 0.05 %. However $\Phi_1(z)$ depends strongly on the length of the cylinders. It changes in present case by almost 1.5 %. The changes in potential functions appeared to be not sufficient to cause a shift in the calculated focal lengths towards those calculated by Harting and Read. See again table 4.3.

The differences found with H. and R. are now believed to be caused by the following. In [Har-76] the focal properties are calculated by integration of paraxial ray equation (3.56) for which as axial potential function has been taken:

z/D		0.00	0.05	0.1	0.5	1.0
$\Phi_0(z)$	$N = 32$	0.00000	0.07001	0.14004	0.66937	0.95988
	$N = 56$	0.00000	0.07053	0.14108	0.67257	0.96047
	$N = 84$	0.00000	0.07057	0.14115	0.67270	0.96049
$\Phi_1(z)$	$N = 32$	0.8878	0.8886	0.8907	0.9449	0.9929
	$N = 56$	0.8893	0.8900	0.8921	0.9460	0.9931
	$N = 84$	0.9024	0.9031	0.9050	0.9524	0.9939

Table 4.4 *Axial potential* $\Phi_0(z)$ *and* $\Phi_1(z)$ *for lens* $G = 1.0D$

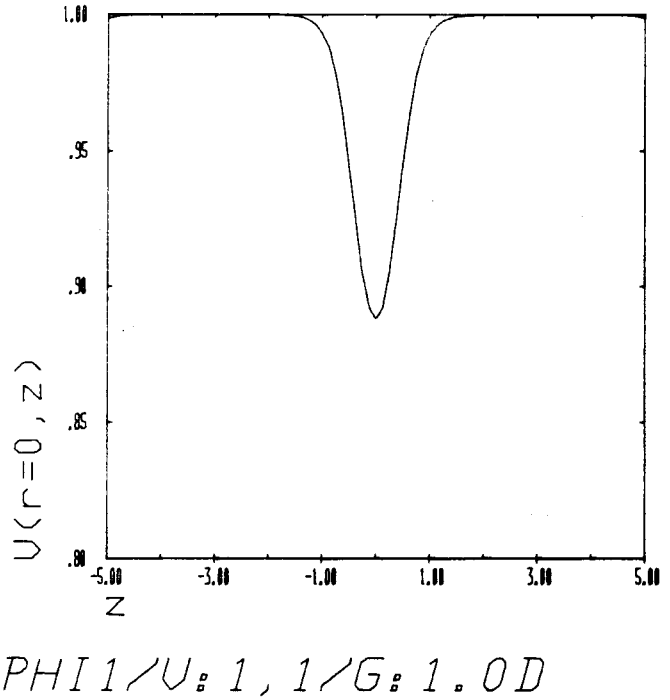

Fig. 4.2 *Axial potential* $\Phi_1(z)$ *for lens* $G = 1.0D$

$$\Phi(z) = \frac{1}{2}(V_1+V_2) + \frac{1}{2}(V_2-V_1)\Phi_0(z). \tag{4.1}$$

(4.1) implicitly contains the assumption that $\Phi_1(z)$ (the axial potential function for the case $(V_1,V_2)=(1,1)$, as already used before) has exactly value 1. However the above listed results (see table 4.4) indicate that this is not true, at least for lenses with cylinder-lengths up to about 10. In order to have better evidence that the axial potential used by [Har-76] indeed causes the differences with present results, the trajectory calculations were repeated (for $N=32$) using the paraxial ray equation. In the calculations one time $\Phi_1(z)$ was taken to be equal to 1, and another time calculated values for $\Phi_1(z)$ were substituted. It appeared to be difficult to integrate the paraxial ray equation with such an accuracy that the focal lengths had an accuracy of three digits. Because of the (implicit) discontinuity of the second derivative in the axial potential function the accuracy demand in the integrator-subroutine had to be chosen with great care. The focal properties finally found are shown in table 4.5.

$\frac{V_2}{V_1}$	N = 32 $\Phi_1(z)$ calculated				N = 32 $\Phi_1(z)$ = 1			
	f_1	F_1	f_2	F_2	f_1	F_1	f_2	F_2
5.0	2.65	4.13	5.90	3.72	2.56	4.09	5.79	3.58
10.0	1.16	2.32	3.62	1.66	1.11	2.32	3.53	1.55
20.0	0.64	1.72	2.82	0.83	0.60	1.70	2.69	0.71
40.0	0.40	1.43	2.49	0.34	0.38	1.43	2.38	0.26
80.0	0.27	1.30	2.44	0.00	0.26	1.30	2.33	-0.06

Table 4.5 *Focal lengths for lens $G = 1.0D$. present results, using paraxial ray equations*

Although the effect of taking $\Phi_1(z) = 1$ on F_1, which already had a relatively good agreement with the H. and R. values, is not clear, the effect on f_1 (especially at the lower voltage ratios), f_2 and F_2 is evident. E.g. whereas f_2 previously disagreed by up to 3 % with the H. and R. values, the difference when $\Phi_1(z) = 1$ has a maximum of about 1 %.

Now that the focal properties have been calculated using both the original equations of motion and the paraxial ray equation, it is interesting to compare the computer times taken by the respective methods. Calculating the trajectories from the equations of motion required, for a lens of only 32 segments, more than a minute each trajectory. The requirements when using the paraxial ray equation are minimal compared with this. After $\Phi_0(z)$ and $\Phi_1(z)$ have been calculated once each trajectory takes only about one second.

4.2 3-element aperture lens

To have better evidence that the charge density method as used gives correct results, the method also has been tested on more complicated lenses. One of them was a cylinder-symmetrical 3-element aperture lens with a gap A : aperture diameter D ratio of 0.5, and with an aperture thickness of $0.05D$. The lens was shielded by cylinders of diameter $5D$ at the first and third electrode. The electrodes were divided into a total number of $N = 63$ segments. Ion trajectories were calculated by direct solution of the equations of motion. Some results of calculated focal lengths are shown in table 4.6.

$\frac{V_2}{V_1}$	present results $N = 63$		[Har-76] $N = 560$	
	f_2	F_2	f_2	F_2
-0.9	0.40	0.04	0.40	0.03
-0.5	1.19	1.12	1.18	1.11
-0.3	2.04	2.00	2.02	1.98
0.0	4.67	4.65	4.65	4.63
5.0	2.80	2.74	2.77	2.71
10.0	1.58	1.38	1.57	1.37
20.0	1.31	0.81	1.32	0.78
40.0	1.56	0.21	1.59	0.16

Table 4.6 *Focal lengths for lens $A = 0.5D$. $V_3/V_1 = 1.0$*

Listed values are for the situation in which the lens is used as an einzel lens, i.e. energy

before and after passing the focal region is equal. Then besides $f_1 = f_2$ and $F_1 = F_2$. As can be seen from table 4.6 there is a good agreement with the results in [Har-76]. The deviation when V_2/V_1 is caused by the circumstance that in present situation the trajectory integration was stopped at $z = 6$, whereas there for V_2/V_1 the ion had not reached its asymptotic path yet.

4.3 EARISS zoom lens

model for calculations

Largest part of the lens properties which will be presented in this section have been calculated using a model for the electrodes as shown in azimuthal cross-section in figure 4.3. For the calculation of the charge density the electrodes shown were divided into segments of widths varying from 0.22 mm up to 2.4 mm. The total number of segments N was 293 then.

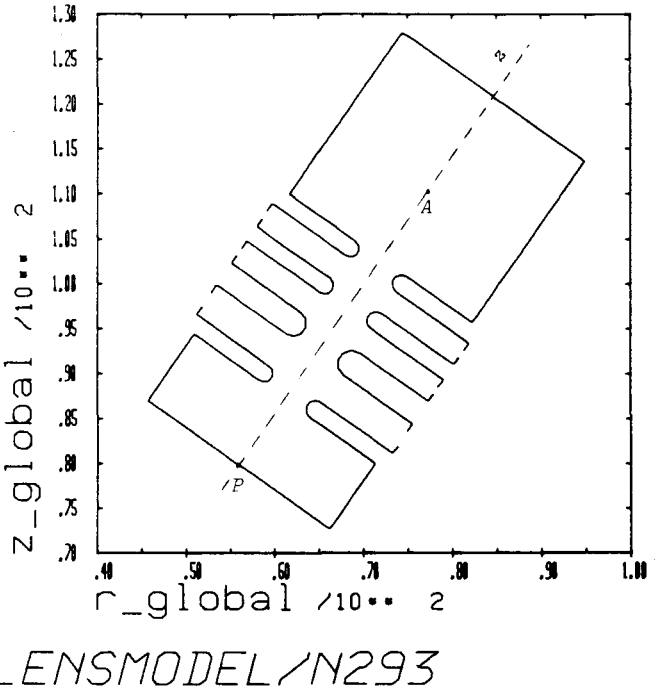

Fig. 4.3 *Azimuthal cross-section of the zoom lens model used in the calculations*

Calculation of the charge density with this segmentation, for three independent combinations of electrode potentials, required a computer storage of 2.3 Mbyte and a computing time of 65 minutes. For some tests a model with $N = 414$ was applied. For this model the requirements were 4.3 Mbyte storage and 2.3 hours computing time.

Figure 4.3 differs from figure 2.5.a, in which the actual geometry of the lens is shown, with respect to the following three aspects.

a. The curvature of the electrode-endings in the gap has been approximated by a number of five chords in stead of by half a circle. However it is expected that because of the small angle (36 °) between neighbouring chords and the small maximum distance among the chords and the circle-half (< 0.04 mm) this approximation will give a negligible error in the calculated lens properties. This seems to be confirmed by results of calculations with the $N = 414$ model, in which seven chords replace the five chords of $N = 293$ and in which besides a smaller minimum segment width (0.15 mm) is used. Plots of trajectories for $N = 414$, drawn at a normal scale, are indistinguishable from those for $N = 293$. At the risk of labouring the obvious as a further check the potential at the z-axis for the five chords model was compared with that for the seven chords model. Some results have been listed in table 4.7.

V_1,V_2,V_3,V_4	0.0,0.0,1.0,1.0		0.0,0.0,1.0,2.0	
N \ z	22.0	24.5	22.0	24.5
293	0.6636	0.4502	1.01164	1.45945
414	0.6642	0.4504	1.01155	1.45961

Table 4.7 *Axial potentials in the gap among the electrodes for a more ($N = 414$) or less ($N = 293$) accurate model. all potentials in the same units*

$z = 22$ mm is the position at the third electrode, $z = 24.5$ mm is half-way the third and the fourth electrode. The differences in potential between $N = 293$ and $N = 414$ in table 4.7 have a maximum of 0.1 % or 0.0006 kV (when electrode potentials are in kV). The differences in magnitude and angle of the electrical field, which have not been listed, are 0.0003 kV/mm and 0.1 ° at most.

b. In figure 4.3 the ends of the gaps among the electrodes have been closed for a part using cylinder segments at $z = 13.5$ mm ($= 2.7\,H$). N.B. in three-dimensional space these segments are parts of a cone. In reality there is no such closing but the electrodes extend a longer distance in r-direction, though it is with a corner in them (see figure 2.5.a). No doubt the electrodes in figure 4.3 have an expanse in r-direction enough to give correct near-axial fields. Tests did show leaving out the closings had no influence on the calculated focal properties.

c. In figure 4.3 both the front-side (small z) and the back-side (large z) of the lens have been closed using longish closing boxes. The one at the front-side extends up to the pupil ($z = 0$ mm), the one at the back-side up to 2 H in the analyser ($z = 50$ mm). These boxes have been added to obtain field-free regions at the endings of the lens. For these are necessary to make possible the definition and calculation of focal lengths. Into the region at the fourth electrode which is meant to be field-free in principle fields from the third electrode and from the analyser will penetrate. In practice the analyser is operated in such a way that the potential at the main path s_0 (see figure 1.3) inside it is very close to the initial value of the fourth electrode's potential [Hel-86]. So it is quite acceptable to extend the fourth electrode in z-direction. The only objection against the model for the fourth electrode could be that the second aperture, which is in fact a so-called Herzog-correction element for the analyser, has been dropped. This could result in more field penetration from the third electrode into the fourth one. But tests did show that e.g. at $z = 31$ mm, i.e. halfway the authentic fourth electrode, the axial potential differs only up to a maximal value of 0.1 kV from the potential at the fourth electrode when the third electrode is operated at potentials differing by up to a maximal value of 4 kV from the potential at the fourth electrode. The electric field at that position then has values up to 0.04 kV/mm,

which is small for particles of energy a few keV's.

As with the region in front of the first electrode it is believed to be field-free in good approximation. At the far side with respect to the central axis of the experimental setup the region is screened by the pupil-electrode. At the other side there is screening by an electrode at target potential of einzel lens B (figure 1.3) and by again the pupil-electrode. By the way, if space in front of the first electrode would be completely empty, an ion starting from the position of the target would not go along a straight trajectory towards the opening of the zoom lens. In preliminary calculations it was found that then the trajectory is influenced by a kind of dipole-field.

calculation of focal properties

In the first instance a large number of paraxial trajectories was calculated for the standard model ($N=293$) by a direct solution of the equations of motion as described in section 3.4.1. Each trajectory costed more than 20 minutes computing time, with an average of 85 field evaluations. Some results for the trajectories of ions which start in a direction parallel to the z-axis are shown in appendix A in figures a.1.a up to a.1.d inclusive and in figure a.2. Figures a.1 are for the $V_4/V_1=2.0$ case, figure a.2 for $V_4/V_1=6.0$. The choice of the $(V_2/V_1, V_3/V_1)$ combinations in the shown figures is not quite arbitrary, as will be clear when reading following section concerning the lens as a zoom lens.

Most striking in shown figures is that the focal points don't coincide with the z-axis but lie below, i.e. in the direction of the central axis of the apparatus. Obviously there is no optical axis which coincides with the geometrical z-axis. Nor the radial position r_F of the calculated focal points with respect to the z-axis is constant either. r_F appeared to vary between -0.03 mm and -0.01 mm. Further the position of the principle planes, and so the magnitude of f_1 and f_2 cannot be determined accurately. Of course non-paraxial trajectories could have been used for the determination of the focal properties, but then possibly the results should have been influenced by the occurrence of spherical aberrations. In a further section there will be returned to the occurrence of spherical aberrations. The focal lengths which can be derived from figures a.1 and a.2 have been listed in table 4.8.

$\frac{V_2}{V_1}$	$\frac{V_3}{V_1}$	$\frac{V_4}{V_1}$	$\bar{f}_1$	F_1	$\bar{f}_2$	F_2	Δf_1	Δf_2	$\frac{\bar{f}_2/\bar{f}_1}{\sqrt{V_4/V_1}}$
2.0	0.5	2.0	2.40	3.06	3.46	2.20	0.4	0.4	1.02
2.5	4.5	2.0	3.06	4.60	4.48	1.00	0.16	0.02	1.04
0.5	1.5	2.0	2.26	4.04	3.26	1.86	0.02	0.02	1.02
0.5	0.5	2.0	1.60	2.44	2.20	1.68	0.06	0.06	0.97
2.0	2.5	6.0	2.06	4.50	4.86	1.60	0.10	0.16	0.96

Table 4.8 *Focal lengths derived from figures a.1 and a.2 (appendix A). for trajectories calculated by direct solution of equations of motion. focal lengths are in units H*

F_1 and F_2 are measured with respect to $z=22$ mm, which is the position in the middle of the third electrode. $\bar{f}_1$ and $\bar{f}_2$ are mean values of f_1 and f_2 respectively for $r_0=0.03$ mm and $r_0=-0.07$ mm, where r_0 is the radial position with respect to the z-axis at the beginning of the trajectory. Δf_1 and Δf_2 denote the deviation from the mean values for these r_0. $\bar{f}_2/\bar{f}_1$ disagrees by up to 4 % with the theoretic $(V_4/V_1)^{1/2}$.

However the accuracy of $\bar{f}_1$ and $\bar{f}_2$ may be, the computer time for each trajectory is far too large to be able to study systematically the possibilities of the lens as a zoom lens. For this reason in section 3.4.2 a paraxial ray equation was derived. In view of the above noticed shift of the focal points an axis which lied 0.02 mm below the z-axis was taken to

expand the potential around, for three independent combinations of electrode potentials. Results of trajectory calculations using the paraxial ray equation can also be found in figures a.1 and a.2 of appendix A. Calculation of these trajectories only required a computer time of about one second each trajectory. New calculated focal lengths are shown in table 4.9.

$\frac{V_2}{V_1}$	$\frac{V_3}{V_1}$	$\frac{V_4}{V_1}$	$r-r_0 = 0.03$ mm					$r-r_0 = 0.05$ mm				
			f_1	F_1	f_2	F_2	$\frac{f_2/f_1}{\sqrt{V_4/V_1}}$	f_1	F_1	f_2	F_2	$\frac{f_2/f_1}{\sqrt{V_4/V_1}}$
2.0	0.5	2.0	2.37	2.89	3.42	2.19	1.02	2.38	2.90	3.34	2.19	0.99
2.5	4.5	2.0	3.07	4.76	4.45	1.10	1.02	3.10	4.66	4.42	0.98	1.01
0.5	1.5	2.0	2.29	3.97	3.33	1.89	1.03	2.30	3.99	3.19	1.77	0.98
0.5	0.5	2.0	1.57	2.40	2.17	1.65	0.98	1.55	2.38	2.20	1.66	1.00
2.0	2.5	6.0	1.97	4.36	4.83	1.63	1.00	1.99	4.47	4.84	1.62	0.99

Table 4.9 *Focal lengths for the voltage ratio combinations of figures a.1 and a.2 (appendix A). for trajectories calculated with a paraxial ray equation. focal lengths are in units H*

The agreement with focal lengths from former calculations, see table 4.8, is surprisingly good.

The relevance of the obtained focal lengths for further calculations can be checked to a certain extent in following way. When tracing trajectories by direct solution of the equations of motion for given object distance z_p the conjugate image distance z_q is found, and vice versa. The (z_p, z_q) combination found is to be compared with the (z_p, z_q) combination which is obtained from direct matrix-calculation using the calculated focal lengths. An example of an (z_p, z_q) combination obtained from direct ray tracing is shown in figure 4.4. Starting at $z_q = 2.8\,H$ for the voltage ratio combination $(V_2/V_1, V_3/V_1, V_4/V_1) = (1.0,5.0,3.0)$ $z_p = -5.0\,H$ is found. The focal lengths calculated in paraxial approximation give for the same voltage ratio combination $(z_p, z_q) = (-5.04,2.8)$. Tests for a few other combinations did show comparable good agreement.

the lens as a zoom lens

In section 2.2 it was described that the considered lens is used as a zoom lens in the EARISS setup. With an object effectively situated at the position of the window independently of the pre-acceleration the image must be kept constant at the position of the analyser entrance. As a function of V_4/V_1 then at least one of the voltage ratios V_2/V_1 and V_3/V_1 must be varied. How the occupied part of phase plane at the position of the analyser would be if V_2/V_1 and V_3/V_1 both had value 1, i.e. if both the second and third electrode were kept at target potential, is shown in figure 4.5. Here for some V_4/V_1-values the phase diagram at the analyser entrance ($z = 37.0$ mm $= 4.4\,H$) has been drawn. It was derived from the focal lengths calculated using the paraxial ray equation. An explanation to figure 4.5 has already been given in section 2.3. For V_4/V_1 near to 1 there is few focusing action and the phase-diagram doesn't rotate enough. For large V_4/V_1 there is strong focusing action and the phase-diagram can even rotate beyond the desired vertical position.

Position z_b, where, for given focal lengths and phase-diagram at the pupil, the phase-diagram will be imaged, i.e. transformed to a vertical one, can easily be derived using matrix equation (2.4). Combination of the equations for u_{b_1} and u_{b_2}, the dimensionless co-ordinates of the transformed rays 1 and 2 from figure 2.3.b, gives when $u_{b_1} = -u_{b_2}$ equation (4.2).

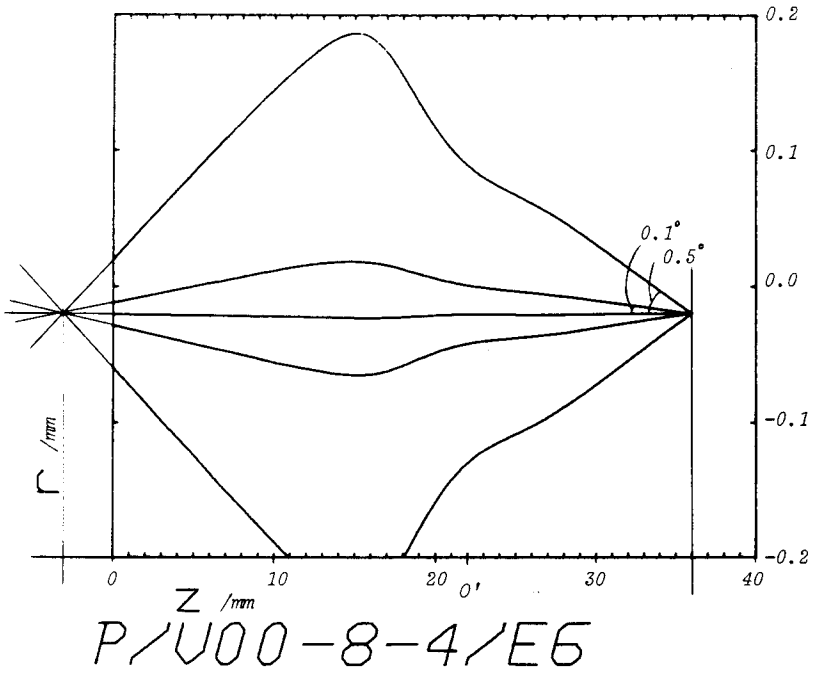

Fig. 4.4 *Conjugate object-image pairs, obtained from trajectory tracing*

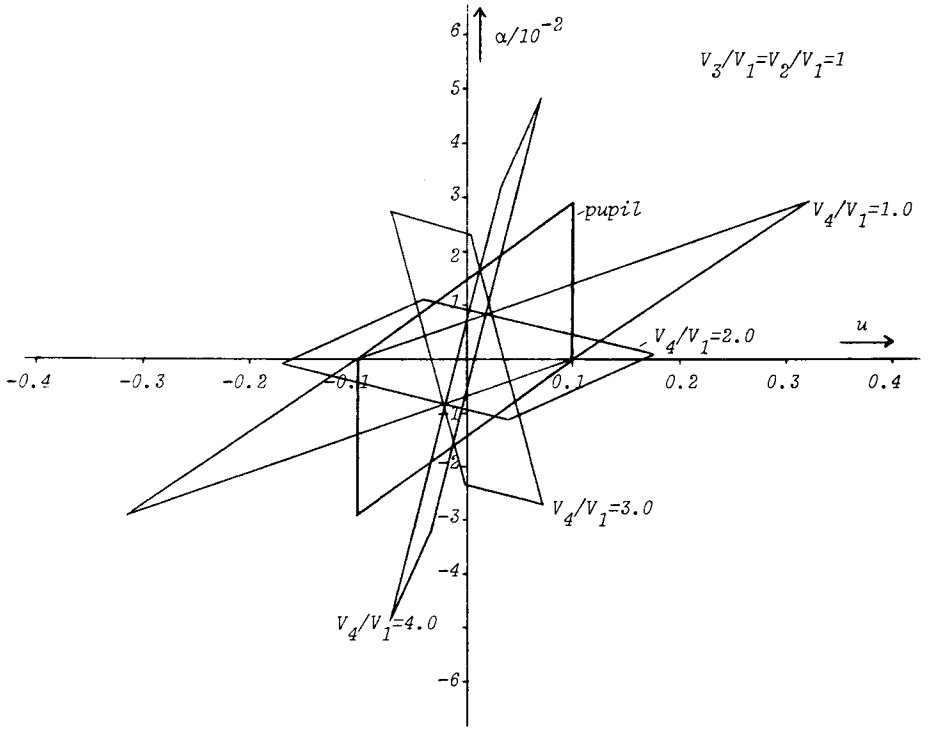

Fig. 4.5 *Phase-diagram at the analyser entrance when* $V_2/V_1 = V_3/V_1 = 1$

$$z_b = f_2\left|1-\frac{f_1(\tan\alpha_{p_1}+\tan\alpha_{p_2})}{(z_v+F_1)(\tan\alpha_{p_1}+\tan\alpha_{p_2})-2u_{p_1}}\right|+p_2 \qquad (4.2)$$

As an alternative z_b could also have been obtained as being the image distance z_q for an object at position $z_p = z_w$, where index w denotes the window.

Using (4.2) in present study a search was made for $(V_2/V_1, V_3/V_1)$ combinations at fixed V_4/V_1 that have a z_b coinciding with z_a. The focal lengths needed were calculated using the paraxial ray equation. For convenience all the time the middle of the third electrode was taken as a reference plane, from which the focal lengths, z_b and z_a were measured (in units H). The desired z_b must be equal to 3.0 then. Results of calculations are shown in figure 4.6.a, in curves which represent $z_b = 3.0$ for different values of V_4/V_1. The curves actually have been found using a computer-program which contains a subroutine for finding zeros. Shown curves have their equivalence in literature as (P,Q)-curves. In present report however they will be defined as zoom lens curves. The behaviour of u_{b_1}, α_{b_1} and α_{b_2} on the curves has been drawn in figures 4.6.b and 4.6.c.

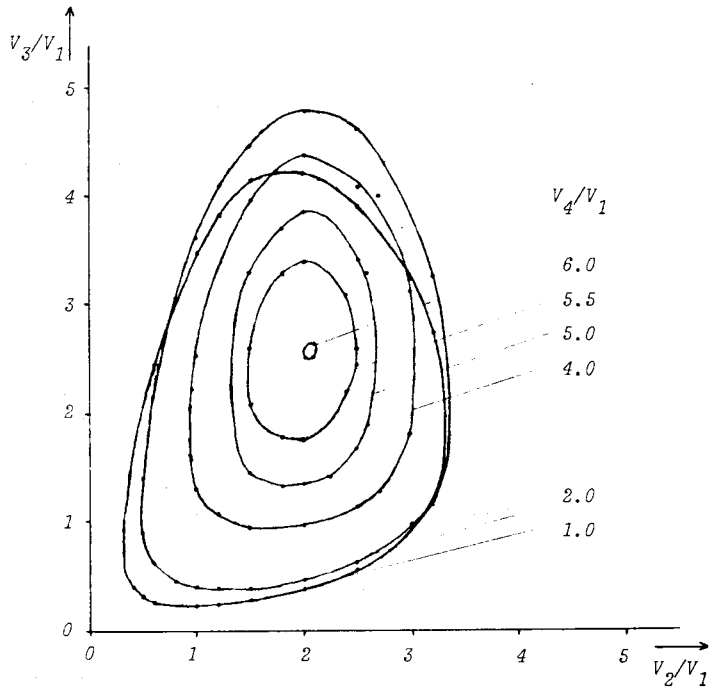

Fig. 4.6.a *Curves representing $(V_2/V_1, V_3/V_1)$ combinations for which $z_b = 3.0\,H$*

Figure 4.6.a can be explained to some extent using a qualitative contemplation in terms of a "movable" lens. If $V_4/V_1 = 1.0$ the lens is an einzel lens per definition. Taking besides one of the voltage ratios V_2/V_1 or V_3/V_1 equal to 1 the lens approximately is a 3-element einzel lens. When neglecting differences in radius of curvature between successive lens elements and differences in gap-width between the electrodes the only difference between $(V_2/V_1 \neq 1.0, V_3/V_1 = 1.0)$ and $(V_2/V_1 = 1.0, V_3/V_1 \neq 1.0)$ is the distance from the lens up to the pupil. In first case the focusing region has shifted most towards the pupil and so then the largest drift space up to the analyser entrance is left for turning the phase-diagram to a vertical one. One can expect in that case also a voltage ratio should be applied which differs less from 1 than in the second case. This is confirmed by figure 4.6.a. When using the "middle" electrode in accelerating mode for $V_3/V_1 = 1.0$ V_2/V_1 must be taken equal to 3.1, whereas when $V_2/V_1 = 1.0$ a higher value is found for V_3/V_1, namely $V_3/V_1 = 3.5$. When using the middle electrode in decelerating mode the adjustments must

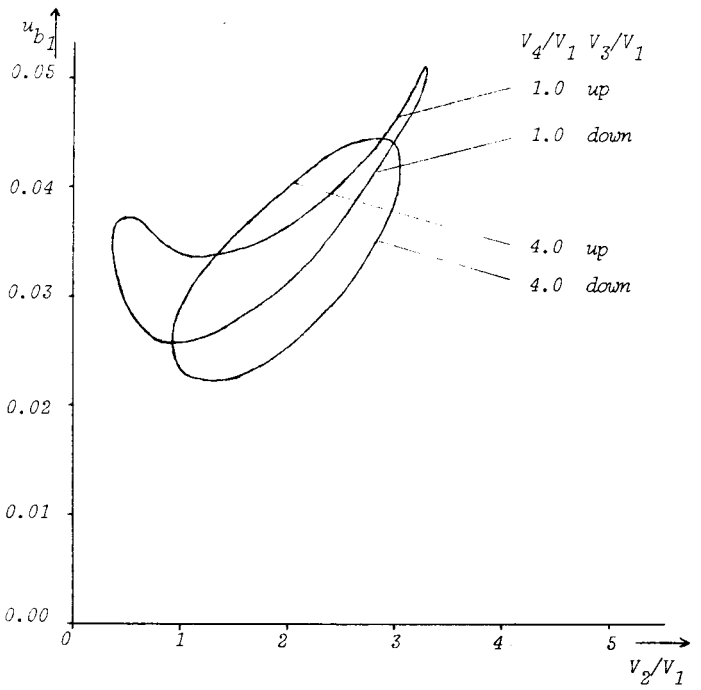

Fig. 4.6.b u_{b_1} *on the curves of figure 4.6.a*

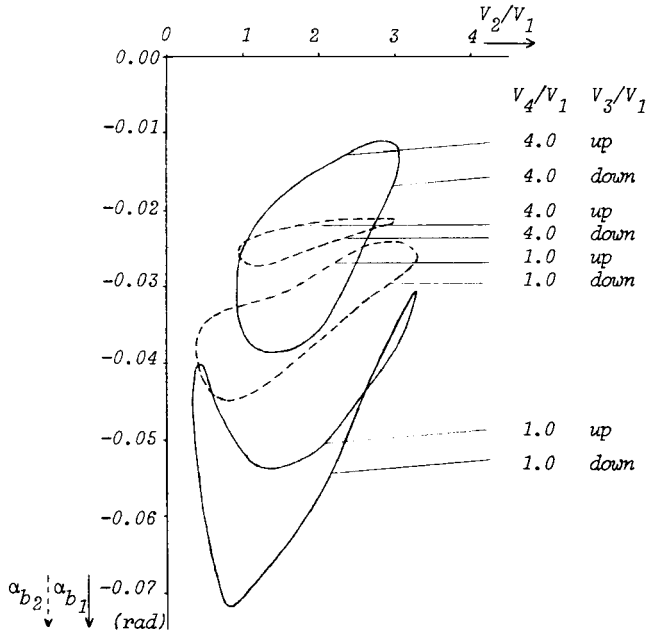

Fig. 4.6.c α_{b_1} *and* α_{b_2} *on the curves of figure 4.6.a*

be $V_2/V_1 = 0.3$ and $V_3/V_1 = 0.2$ respectively. By the way above contemplation only holds if object distance z_p exceeds image distance z_q. Further it has not been studied systematically whether the differences in radius of curvature and in gap width can be neglected. But e.g. in the $V_4/V_1 = 1.0$ case a calculation of the focal lengths for $(V_2/V_1, V_3/V_1)$ = (3.5,1.0) and $(V_2/V_1, V_3/V_1)$ = (1.0,3.5) gives (f_1, F_1, f_2, F_2) = (3.19,3.10,3.16,0.84) and (f_1, F_1, f_2, F_2) = (3.02,2.40,3.04,1.91) respectively. For a clean comparison of F_1 and F_2 they should be measured with respect to the second electrode for the first case. Then they

become $(F_1,F_2)=(2.00,1.94)$.

Let's return to figure 4.6.a. It appears to be that also when using the lens in accelerating mode ($V_4/V_1>1$) the maximal value of V_3/V_1-accelerating is greater than that of V_2/V_1-accelerating. The difference between the minimal V_3/V_1-decelerating and the minimal V_2/V_1-decelerating however is not unambiguous. Further it is found that V_4/V_1 has an upper limit of 6 for present application. When $V_4/V_1=6.0$ V_2/V_1 and V_3/V_1 must be somewhere between 6 and 1, with $V_2/V_1<V_3/V_1$, to decrease the focal strength of the lens at most. More precise values for V_2/V_1 and V_3/V_1 are hard to predict in advance. But in [Har-76] for a planar 3-slit lens following values are given. When $V_4/V_1=6.0$ (N.B. the third electrode now is the last one) focal lengths are at maximum when $V_2/V_1=2.5$. In light of this value combination $(V_2/V_1,V_3/V_1)=(2.0,2.6)$ from figure 4.6.a seems not unreasonable.

Now that zoom lens curves have been found yet an answer must be found to the question which $(V_2/V_1,V_3/V_1)$ combination will be most ideal at given V_4/V_1. The answer will depend on further focal properties like spherical aberrations and magnification and on practical aspects with respect to the operation of the lens.

The occurrence of spherical aberrations has not been investigated systematically in present study. In fact the investigation was confined to calculating changes in focal lengths during variation of the initial distance r_0 to the axis. The calculations were performed by a direct solution of the equations of motion. Only four voltage ratio combinations were tested, all for $V_4/V_1=1.0$. Results of the trajectory calculations are shown in figures b.1. in appendix B. Focal lengths which can be derived from the figures when $r_0=0.5$ mm are listed in table b.1. For comparison the paraxial focal lengths and associate z_b values have also been listed there. A conclusion that can be drawn seems to be that for $V_2/V_1=1.0$ the aberrations are minimal when the third electrode is used in accelerating mode. This conclusion is supported by literature [Rea-70] in which for a 3-element lens in the area about $V_3/V_1=1$ relatively smallest aberration coefficients were found when using the middle electrode in accelerating mode. The figures in appendix B give few further information. Only it appears that in fact the changes in z_b when increasing r_0 are relatively small ($<0.1\,H$).

Although from the above hardly any tangible information about the aberrations is obtained, it must be expected that when operating the zoom lens in EARISS aberrations will be of minor importance. For because of the selecting action of the window-pupil combination the maximum distance to the z-axis will stay small in comparison to the slit height in the electrode. Except when the first electrode passed has a strongly decelerating potential the maximum distance to the axis will be about $0.1\,H$. Trajectories with $r_0=1.0$ mm$=0.2\,H$ as shown in figures b.1 are only of academic interest then.

More important for the determination of the operation mode for the lens seem to be the requirements with respect to the linear magnification M. In section 2.2 it was put that the lens should give a minimum linear magnification M. From figure 4.6.b can be concluded that for obtaining minimum M the lens must be operated at approximately lowest V_3/V_1 values of the zoom lens curves shown in figure 4.6.a. However because of the Helmholtz-Lagrange relationship, equation (2.12), a small M gives a large angular magnification M_α. This effect is evident in figure 4.6.c. A large M_α wouldn't give problems if not the fact is there that the EARISS analyser transforms a vertical phase-diagram at its entrance to a again a vertical phase-diagram at the detector only if in the first phase-diagram $\alpha_{max}<0.03rad$ ([Hel-86]). For greater α_{max} the top of the transformed phase-diagram curves towards the u-axis. For this reason, especially at low V_4/V_1 values, large parts of the $V_2/V_1,V_3/V_1$ curves shown in practice cannot be applied. E.g. for $V_4/V_1=1.0$ those combinations for which $0.5<V_2/V_1<2.5$ are certainly not acceptable. V_2/V_1 must be used in a strongly decelerating or accelerating mode then, and further when V_2/V_1 is in decelerating mode V_3/V_1 must be in accelerating mode. For higher

V_4/V_1 above noticed problem diminishes, and from $V_4/V_1 = 4.0$ towards higher values in fact there is no problem at all.

Another reason not to try to achieve the minimum M for each V_4/V_1 value is that the minimum M value is not a constant equal for all V_4/V_1 values. When making an energy scan it is more favourable to have an approximately constant M over the V_4/V_1 values in the energy scan. Some possibilities for energy scans are shown in figures 4.7.a en 4.8.a. Curves shown in figure 4.7.a are for constant V_2/V_1, those in figure 4.8.a for constant V_3/V_1. The associate u_{b_1} has been sketched in figures 4.7.b and 4.8.b.

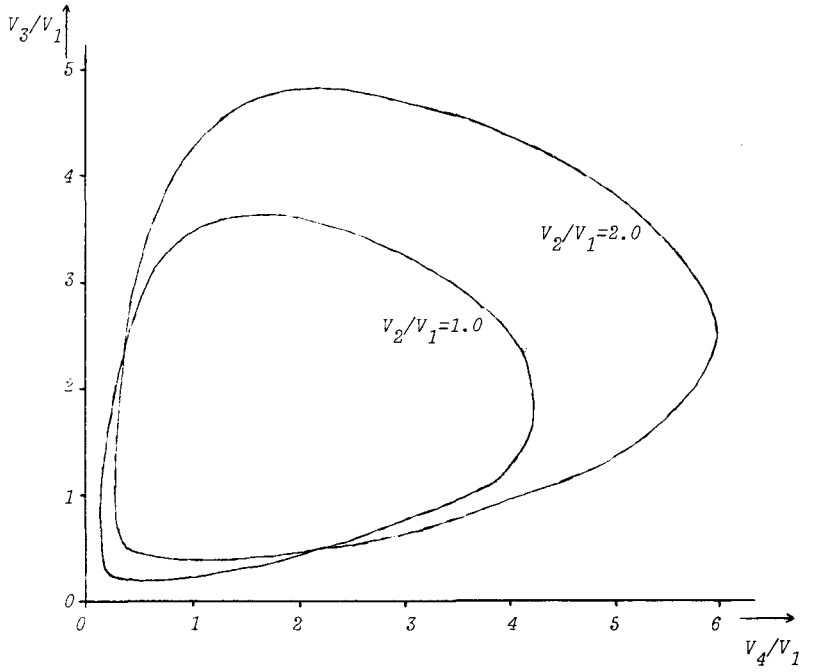

Fig. 4.7.a *Curves representing* $(V_4/V_1, V_3/V_1)$ *combinations for which* $z_b = 3.0\ H$

In the light of the above discussion figure 4.7 in fact is of no practical importance, at least not for $V_4/V_1 < 4$, because then V_2 should be adjusted strongly to obtain a vertical phase plane without a too large angular magnification. But nevertheless certainly the $V_2/V_1 = 1.0$ curve is interesting to show because it can be compared with (zoom lens) curves in literature for three element aperture lenses.

Quite another, practical, aspect when choosing among the possible combinations in figure 4.6 is whether the sign and absolute value of the electrode potentials associate to the voltage ratios shown are desired or even allowed in practical operation of the zoom lens. As with the sign of the potentials there is the complication that it is not possible to reverse the potential of the second and third electrode during an energy (i.e. V_4/V_1) scan. As with the height of the electrode potentials accelerating potentials on the second and third electrode can cause problems, especially at low V_4/V_1. It is just at low pre-accelerations that the scattered ions have highest initial energy. As already noticed before using the third electrode as the controlling electrode for the zooming action requires higher voltage ratios than using the second. How large the associate electrode potentials can be then is shown in following example.
Imagine Ne^+-ions of energy $E_1 = 3$ keV are scattered at a Au-surface. According to equation (1.1) the energy after scattering, for $\theta = 145°$, is $E_3 = 2.07$ keV. It is not unusual to operate the analyser with pass-energy $E_p = 2.5$ keV for this situation. An energy scan is made starting at $V_4/V_1 = 1.0$. Consider the case that both V_2 and V_3 are less than or equal to zero (accelerating mode). Combinations $(V_2/V_1, V_3/V_1) = (1.0, 3.5)$ and $(V_2/V_1, V_3/V_1)$

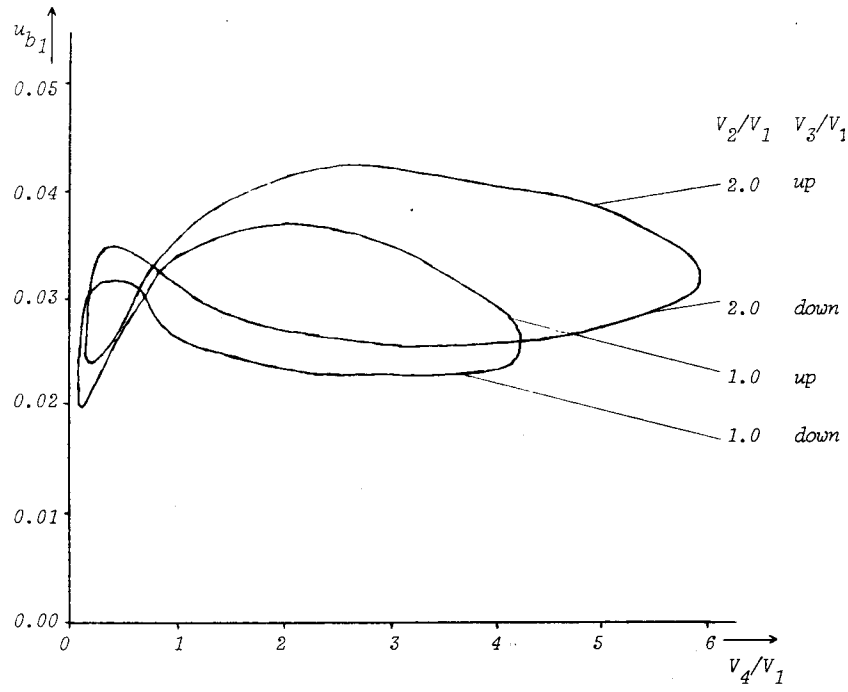

Fig. 4.7.b u_{b_1} *on the curves of figure 4.7.a*

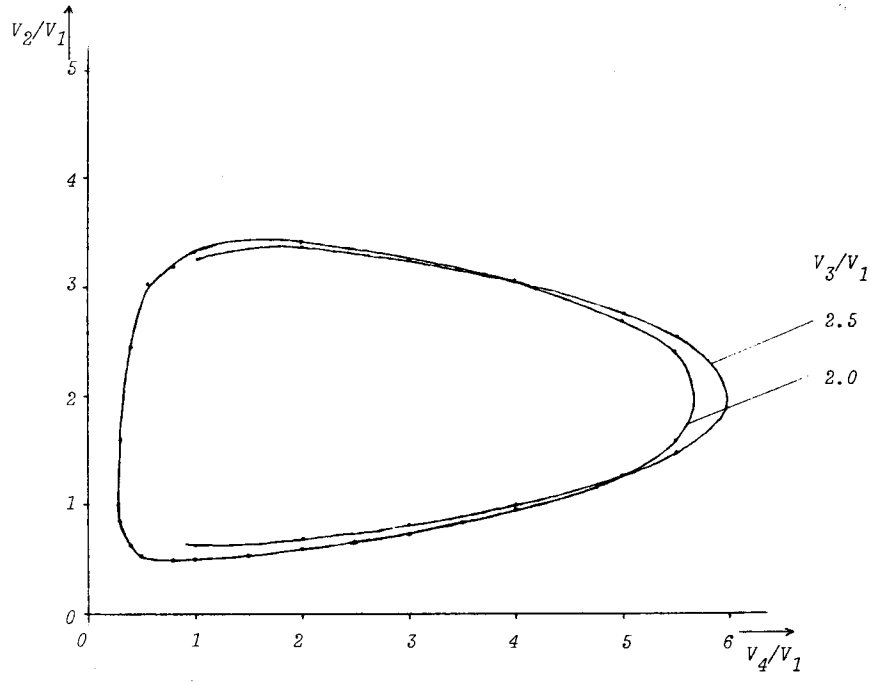

Fig. 4.8.a *Curves representing* $(V_4/V_1, V_2/V_1)$ *combinations for which* $z_b = 3.0\ H$

= (3.1,1.0) for $V_4/V_1 = 1.0$ give potentials $V_3 = -6.25$ kV and $V_2 = -5.25$ kV respectively. Now it is better to use the second voltage ratio than the first. Besides (see section 2.3) the second electrode has a shape which allows the relatively highest field gradients around it.

Another practical aspect is that the adjustment of the electrode potentials should not be critical. With this I mean that e.g. when the lens is operated at given V_4/V_1 a $(V_2/V_1, V_3/V_1)$ combination slightly different from the calculated one must not give a

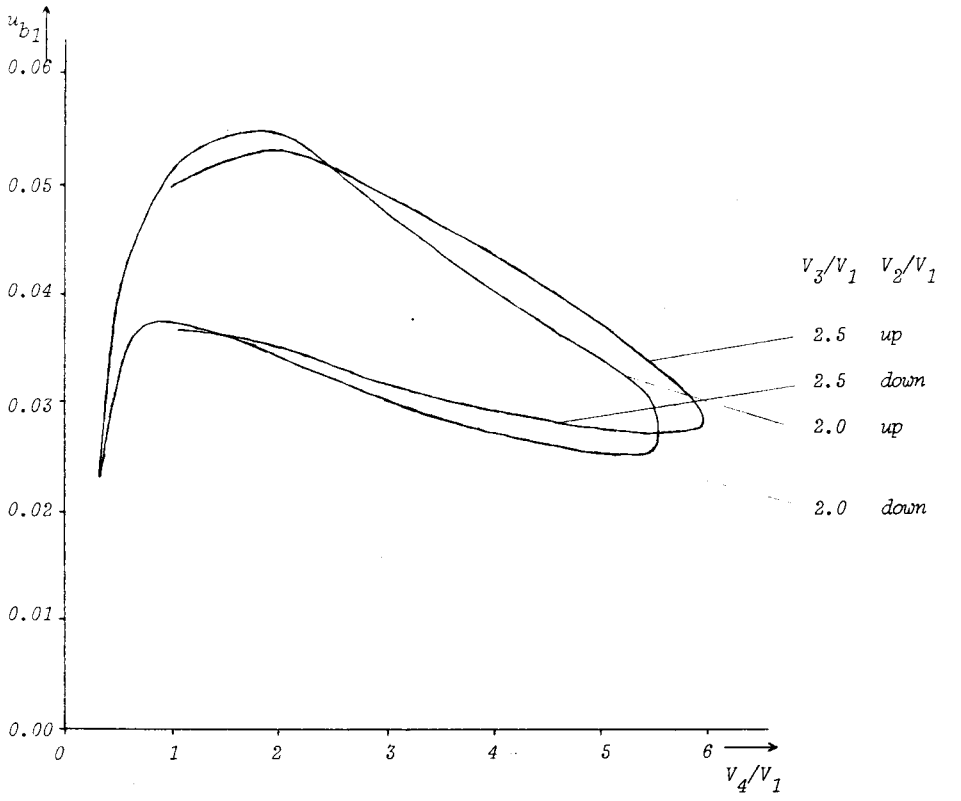

Fig. 4.8.b u_{b_1} *on the curves of figure 4.8.a*

vertical phase-diagram at quite a different z_b. Stated differently, if the calculated $(V_2/V_1, V_3/V_1)$ combinations have a certain unaccurateness it is of importance that they are not in a region in which the partial derivatives of z_b towards V_2/V_1 and towards V_3/V_1 are large.

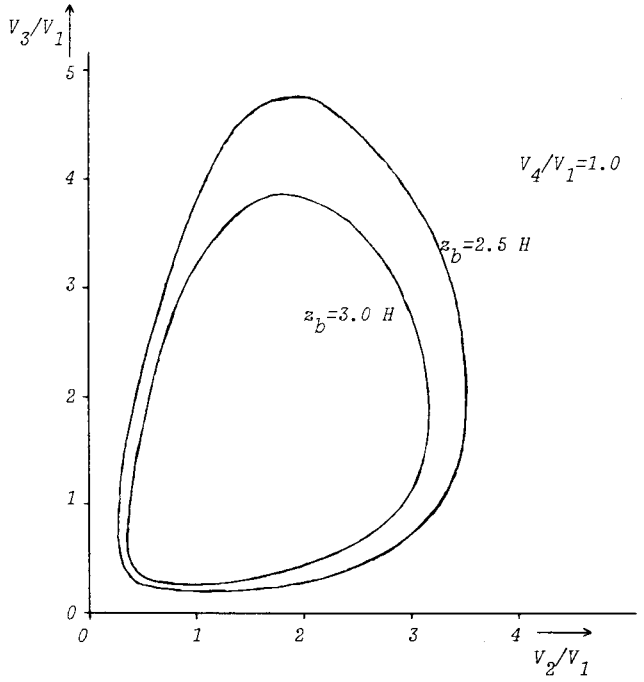

Fig. 4.9 *Curves representing* $(V_2/V_1, V_3/V_1)$ *combinations for which* $z_b = 2.5\ H$ *or* $z_b = 3.5\ H$

From figure 4.9 however it can be seen that, at least in the $V_4/V_1 = 1.0$ case, the zoom lens curves are rather equally spaced. (N.B. V_2/V_1-decelerating and V_3/V_1-decelerating in fact

cannot be expressed accurately in the scale of figure 4.9.) So present aspect seems not to be important.

Above discussion in fact dealt with the adjustment of the lens electrodes when EARISS is used in a scanning mode. When EARISS is operated in such a way, using the multi-detector, that at the same time a considerable part of the whole energy spectrum after scattering is imaged at the detector things are more complicated. As stated before the combination analyser-detector accepts particles of energy $E_p(1-\delta) \leqslant E \leqslant E_p(1+\delta)$. The zoom lens is adjusted for the main energy E_p. For this energy at V_4/V_1 ideal voltage ratios are $V_3/V_1 = (V_3/V_1)_0$ and $V_2/V_1 = (V_2/V_1)_0$. Imagine all voltage ratios are accelerating ones. Ions of lower and higher energy than E_p will undergo greater resp. smaller accelerations for the electrode potentials associated with $(V_4/V_1)_0$, $(V_3/V_1)_0$ and $(V_2/V_1)_0$. For ions of energy $E = E_p(1-\delta)$ following relations can be derived.

$$V_4/V_1 = (V_4/V_1)_0 \frac{1-\delta}{1-(V_4/V_1)_0\delta} \tag{4.3}$$

$$V_3/V_1 = \frac{(V_3/V_1)_0-(V_4/V_1)_0\delta}{1-(V_4/V_1)_0\delta} \tag{4.4}$$

$$V_2/V_1 = \frac{(V_2/V_1)_0-(V_4/V_1)_0\delta}{1-(V_4/V_1)_0\delta} \tag{4.5}$$

E.g. if $(V_4/V_1)_0 = 4$ from (4.3) it appears that $V_4/V_1 = 5$. To obtain the desired focusing also for $E = E_p(1-\delta)$ now a $((V_2/V_1)_0, (V_3/V_1)_0)$ combination should be used which gives a $(V_2/V_1, V_3/V_1)$ combination using (4.4) and (4.5) that is an element of the $V_4/V_1 = 5$ curve. From figure 4.6.a it can be seen that the right side of the $V_4/V_1 = 4$ curve is wrongly situated with respect to the $V_4/V_1 = 5$ curve.

5. Conclusions and discussion

It is believed that the charge density method as used in present report gives accurate results. Calculated lens properties are in good agreement with those available from other authors.

Main objection to present method is that each evaluation of the electric field requires an integration over all electrode surfaces. With a number of segments of about 300 this appears to be a very time-consuming task. It has only been possible to obtain the modes for operating the EARISS zoom lens after expanding the potential around an axis and introducing a suited paraxial ray equation which can calculate the trajectories using the expansion coefficients. To be able to solve the equations of motion efficiently without the need of using paraxial approximations I think the charge density method must be combined with the calculation of the electric fields on a mesh of points about the axis. The mesh needs only extend over the region which is crossed by particle trajectories. To obtain the fields at the mesh points possibly the charge density method can be combined with the finite element method.

The zoom lens appears to be usable for the purpose for which it was designed. Up to pre-accelerations by a factor 6 the scattered ions can be focused in the desired way. Further although there is no optical axis which coincides with the geometrical axis the lens properties can be derived accurately using matrix calculation in phase space.

For low pre-accelerations V_4/V_1 a choice can be made among different V_2/V_1 and V_3/V_1 ratios for the zooming action. Which of them is best is hard to say because many different aspects are of importance. At present stage measurements are needed. In fact during this study already some preliminary measurements have been carried out. But because of a failure in the detection system no differences even between an adjustment with nearly horizontal phase-diagram and one with vertical phase-diagram could be distinguished.

References

[Aar-85] R.G.K.M. Aarts: Berekening van ionenbanen in een elektrostatische ionenlens met behulp van de eindige elementen methode
internal report, Eindhoven University, 1985

[Ack-86] P.A.J. Ackermans: De experimentele bepaling van de oppervlaktesegregatie in Cu-Ni en Pt-Ni legeringen
internal report, Eindhoven University, 1986

[Ban-66] A.P. Banford: The transport of charged particle beams
(E. and F.N. Spon Ltd., London, 1966)

[Boe-83] S.W. Boelens: Het ontwerpen van de versnellens en de azimuth selector voor EARISS
internal report, Eindhoven University, 1983

[Bul-66] R. Bulirsch and J. Stoer: Numerical treatment of ordinary differential equations by extrapolation methods
Num. Math. **8** (1966) 1-13

[Eng-85] J. v. Engelshoven: Theory and implementation of the charge density method
internal report, Eindhoven University, 1985

[Gro-81] H. Groendijk and H.J. v. Kessel: Elektronenoptiek
lecture notes, Eindhoven University, 1981

[Har-76] E. Harting and F.H. Read: Electrostatic lenses
(Elseviers Scientific Publ. Co, Amsterdam, 1976)

[Hel-86] G.J.A. Hellings: Energy and angle resolved ion scattering spectroscopy. new possibilities for surface analysis
dissertation, Eindhoven University, 1986

[Hoo-80] H.A. v. Hoof: A new method for numerical calculation of potentials and trajectories in systems of cylindrical symmetry
J. Phys. E: Sci. Instrum. **13** (1980) 1081-1089

[Jac-62] J.D. Jackson: Classical electrodynamics
(John Wiley and sons, New York, 1962)

[Kas-82] E. Kasper: On the solution of integral equations arising in electron optical field computations
Optik **64** (1983) 157-169

[Kni-83] C.L.C.M. Knibbeler: Ontwikkeling van een twee-dimensionaal plaatsgevoelig detectiesysteem voor het EARISS oppervlakte-analyse apparaat
internal report, Eindhoven University, 1983

[Mul-73] T. Mulvey and M.J. Wallington: Electron lenses
Rep. Prog. Phys. **36** (1973) 347-421

[Nat-72] S. Natali, D. Di Chio, E. Uva and C.E. Kuyatt: Accurate calculation of properties of the two-tube electrostatic lens II: first order focal properties and P-Q curves
Rev. Sci. Instrum. **43** (1972) 80-83

[Pie-83] R. Piessens, E. de Doncker-Kapenga, C.W. Uberhuber and D.K. Kahaner: QUADPACK. a subroutine package for automatic integration
(Springer-Verlag, Berlin, 1983)

[Rea-70] F.H. Read: Asymmetric electrostatic lenses of three apertures
J. Pys. E: Sci. Instrum. **3** (1970) 127-131

[Rea-71] F.H. Read, A. Adams and J.R. Soto-Montiel: Electrostatic cylinder lenses I: two element lenses
J. Phys. E: Sci. Instrum. **4** (1971) 625-632

[Ren-82] A. Renau, F.H. Read and J.N.H. Brunt: The charge-density method of solving electrostatic problems with and without the inclusion of space-charge
J. Phys. E: Sci. Instrum. **15** (1982) 347-354

[Sha-75] L.F. Shampine and M.K. Gordon: Computer solution of ordinary differential equations; the initial value problem
(W.H. Freeman, San Francisco, 1975)

[Sha-76] L.F. Shampine, H.A. Watts and S.M. Daveport: Solving nonstiff ordinary differential equations - the state of the art
SIAM Review **18** (1976) 376-411

[Vel-80] G.W. Veltkamp and A.J. Geurts: Numerieke methoden
lecture notes, Eindhoven University, 1980

[Vor-74] H.A. v. der Vorst: Vergelijking van programmatuur in algol en fortran voor automatische integratie
ACCU-reeks 12, RU Utrecht, 1974

Appendix A

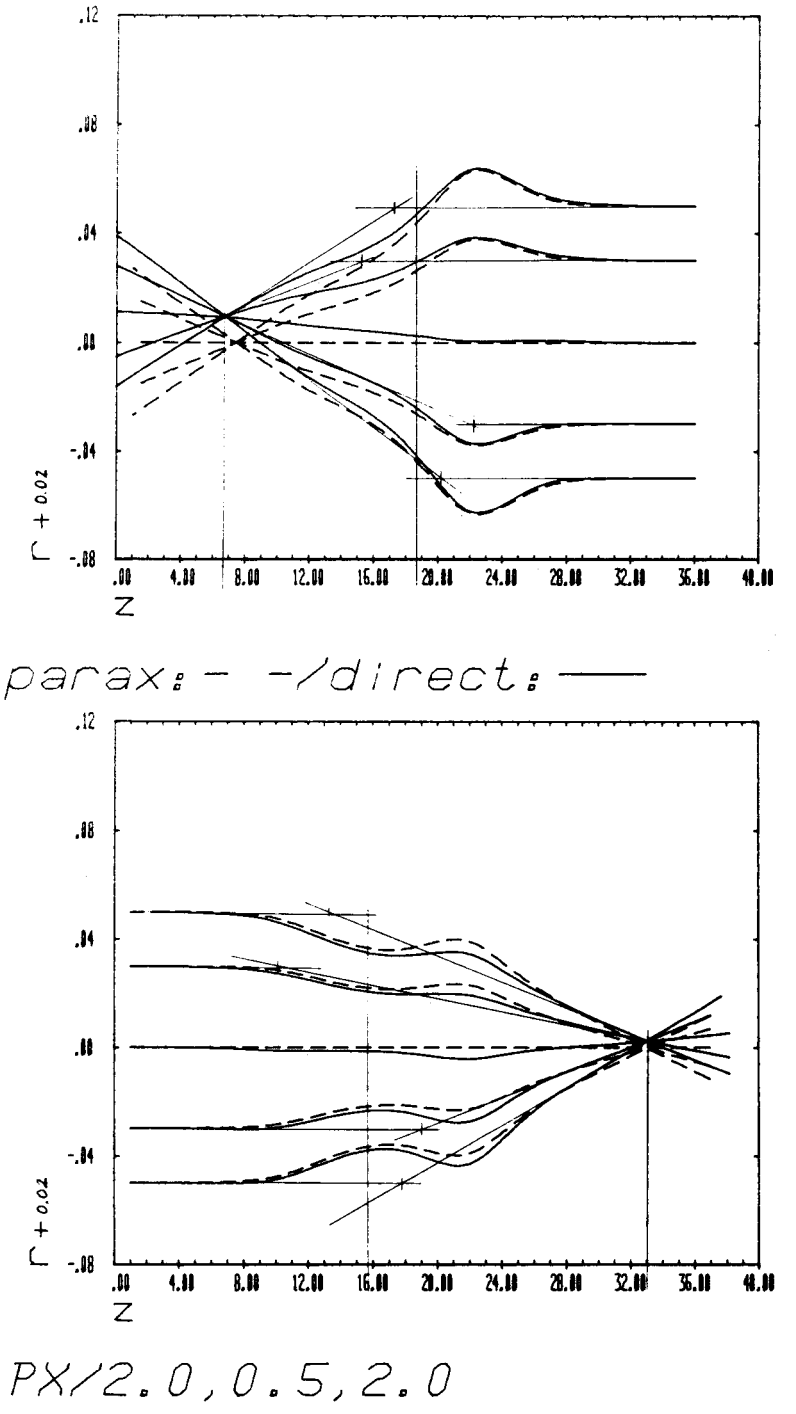

Fig. a.1.a *Paraxial trajectories in EARISS zoom lens, both from a paraxial ray equation and from a direct solution of the equations of motion.* $(V_2/V_1, V_3/V_1, V_4/V_1) = (2.0, 0.5, 2.0)$

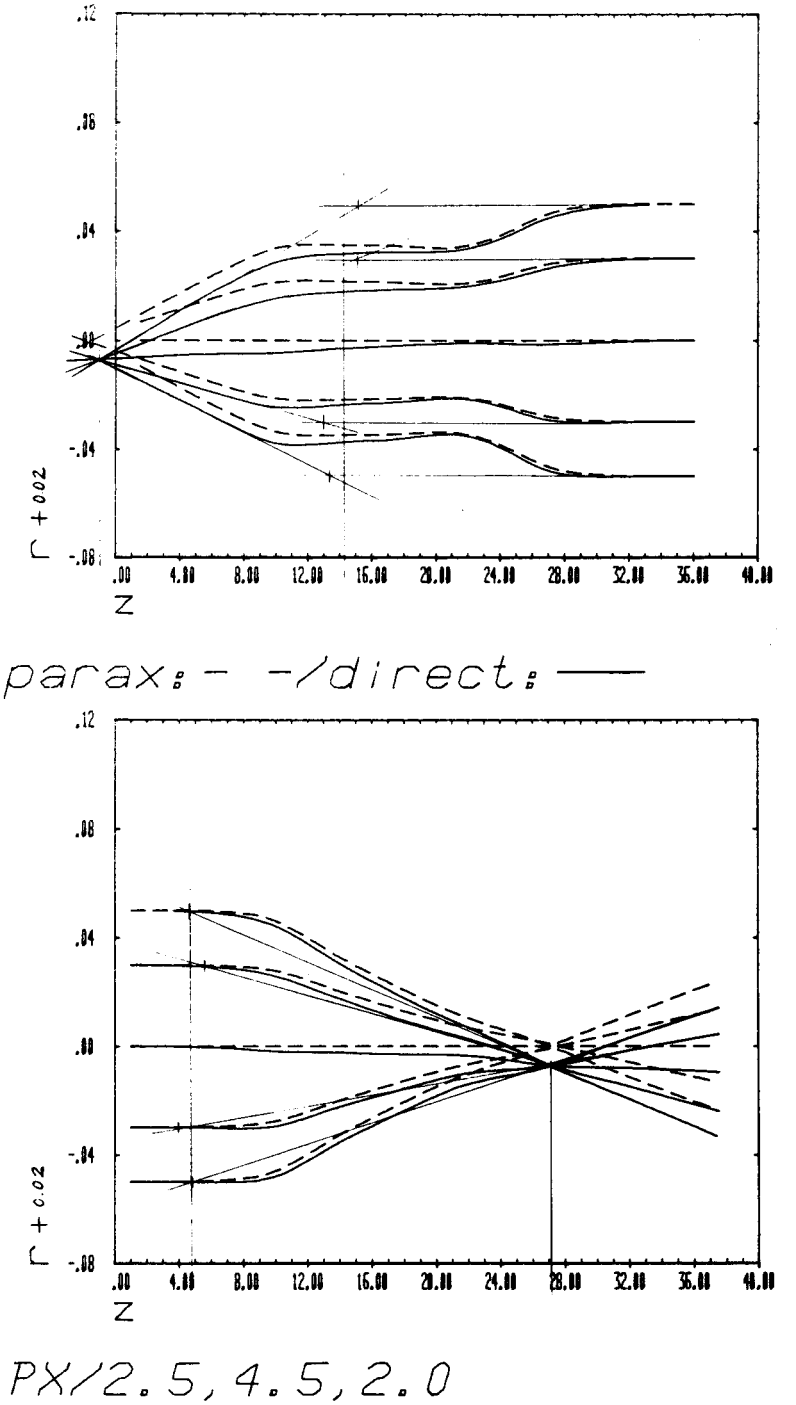

Fig. a.1.b *Idem.* $(V_2/V_1, V_3/V_1, V_4/V_1) = (2.5, 4.5, 2.0)$

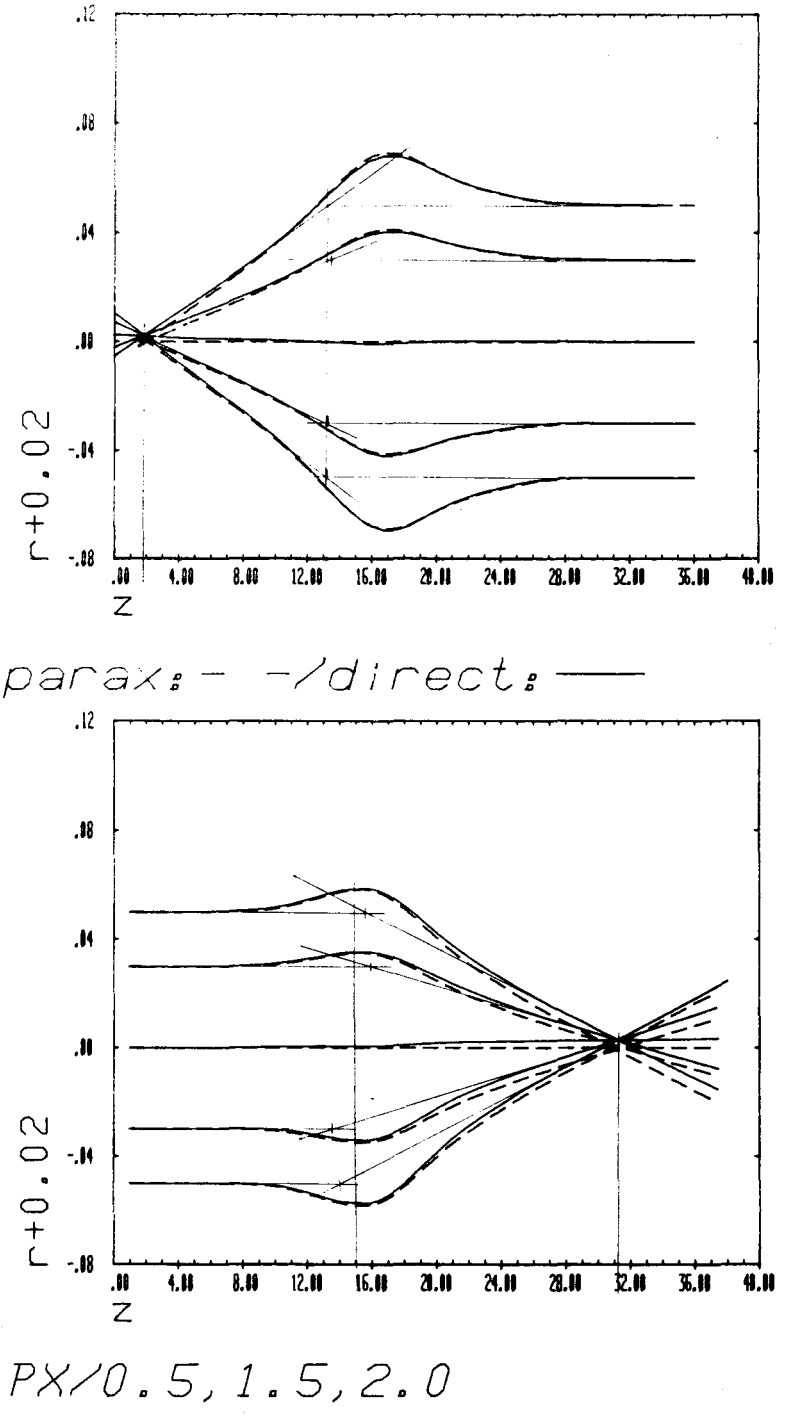

Fig. a.1.c *Idem.* $(V_2/V_1, V_3/V_1, V_4/V_1) = (0.5, 1.5, 2.0)$

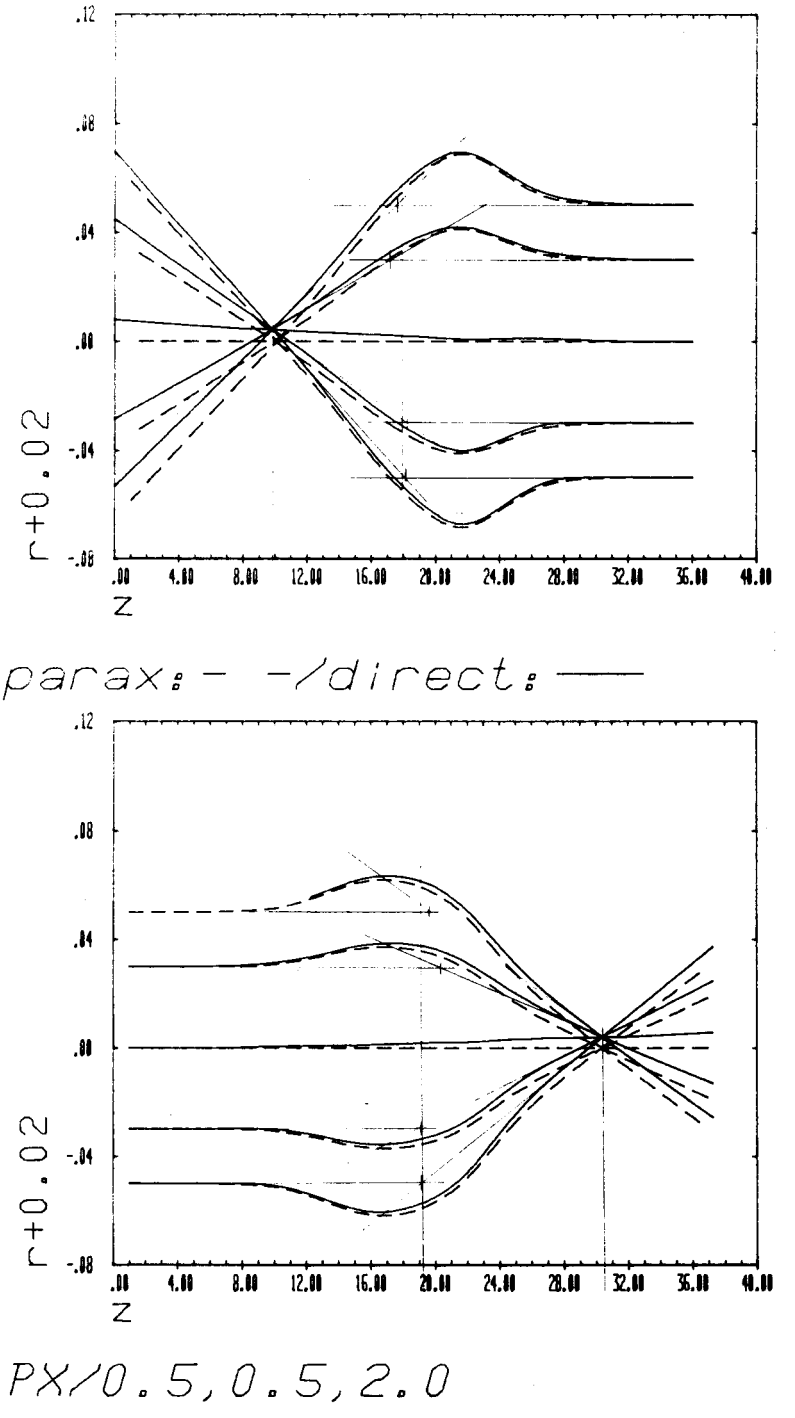

Fig. a.1.d *Idem.* $(V_2/V_1, V_3/V_1, V_4/V_1) = (0.5, 0.5, 2.0)$

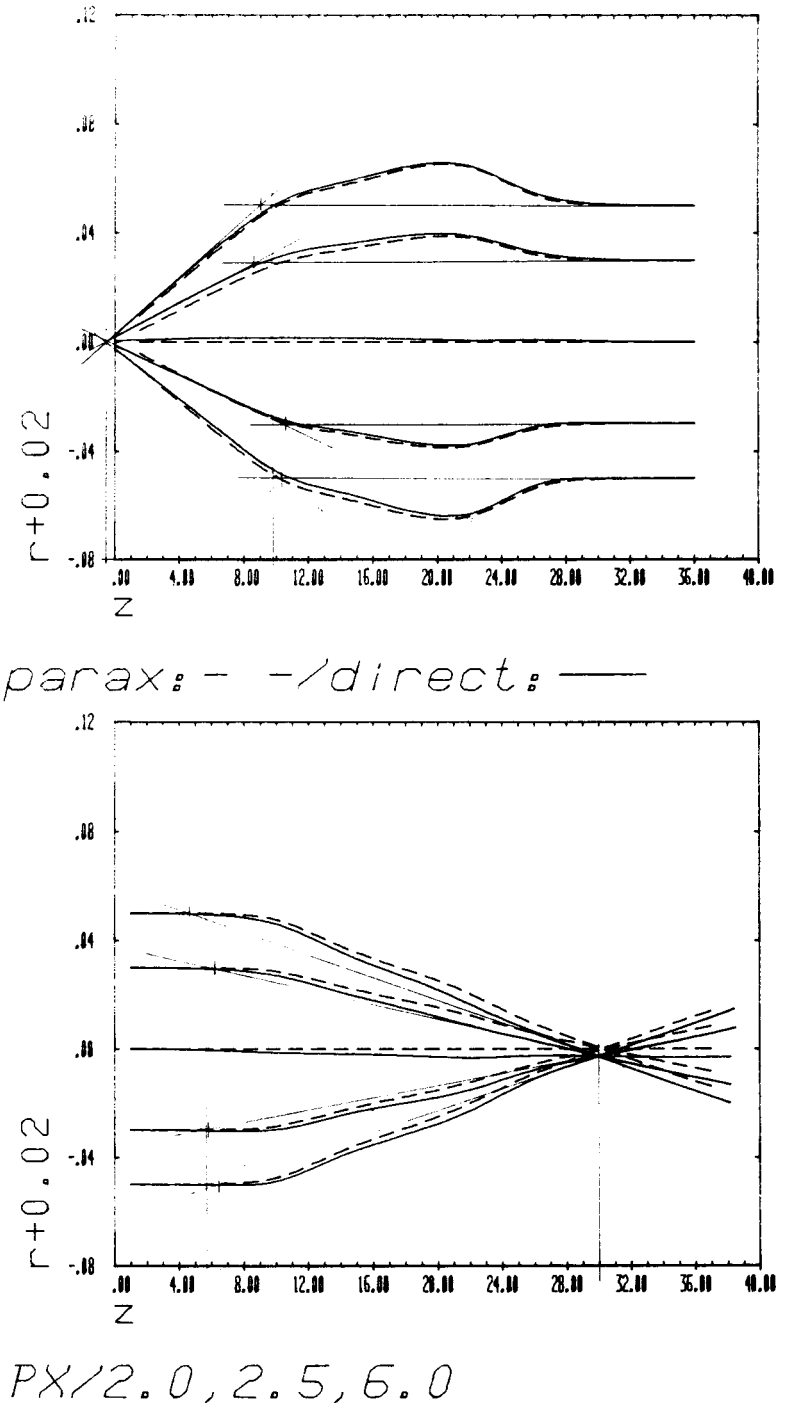

Fig. a.2 *Idem.* $(V_2/V_1.V_3/V_1.V_4/V_1) = (2.0,2.5,6.0)$

Appendix B

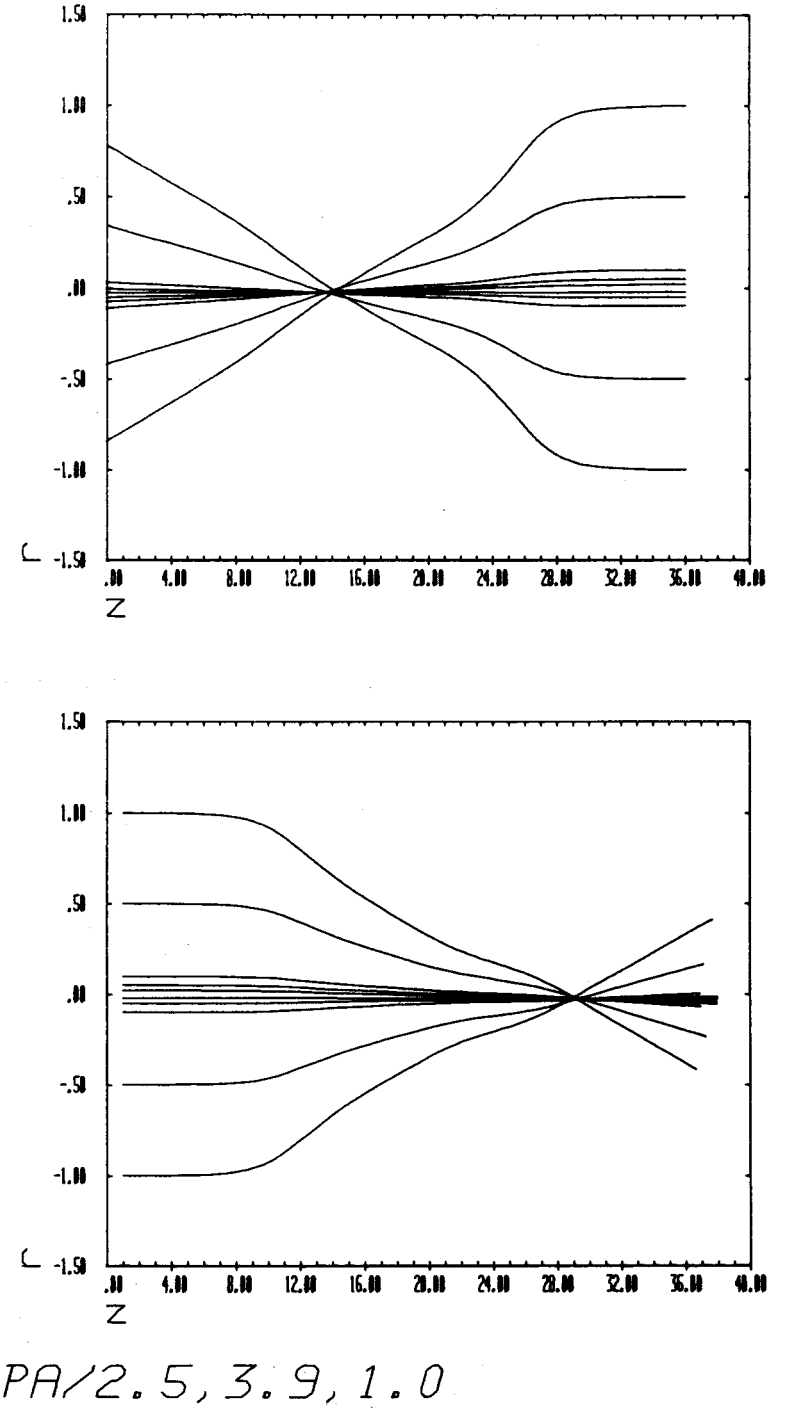

Fig. b.1.a *Paraxial and non-paraxial trajectories in EARISS zoom lens.* $(V_2/V_1, V_3/V_1, V_4/V_1) = (2.5, 3.9, 1.0)$

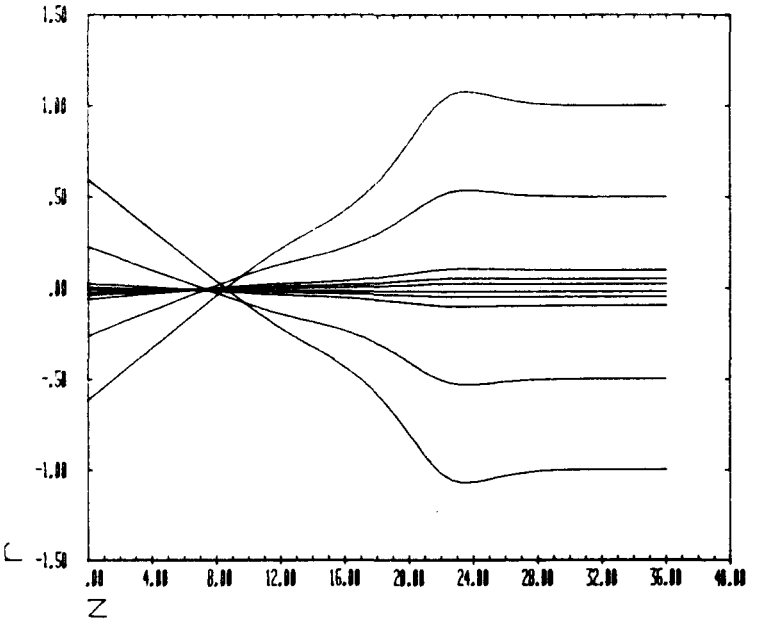

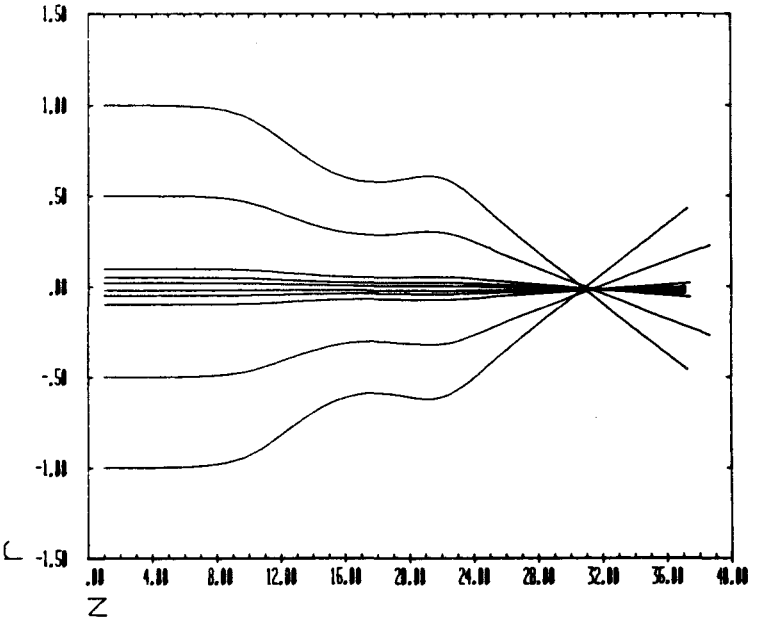

PA/2.5,0.55,1.0

Fig. b.1.b *Idem.* $(V_2/V_1.V_3/V_1.V_4/V_1) = (2.5,0.55,1.0)$

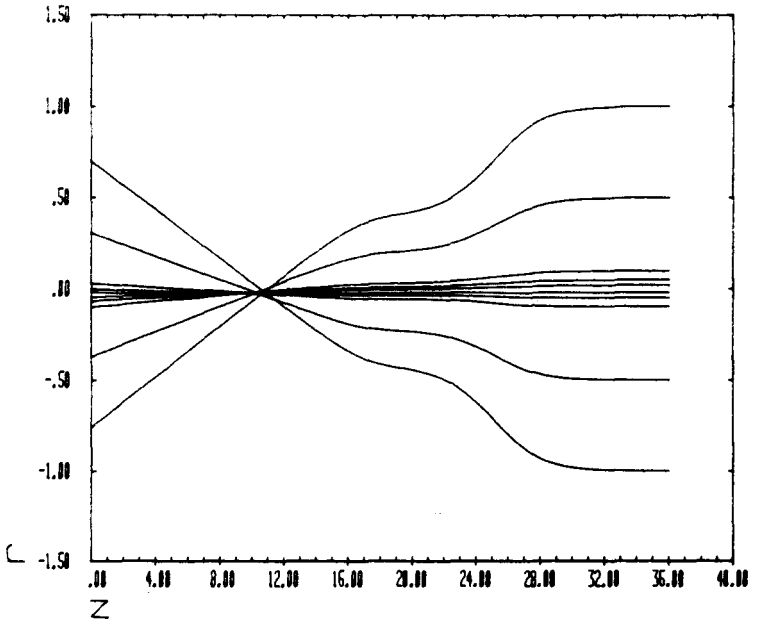

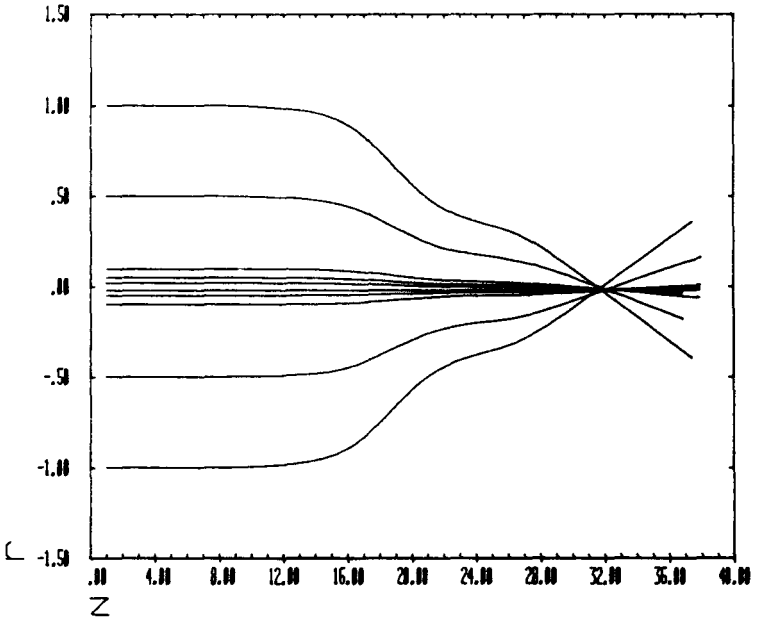

PA/1.0,3.45,1.0

Fig. b.1.c *Idem.* $(V_2/V_1, V_3/V_1, V_4/V_1) = (1.0, 3.45, 1.0)$

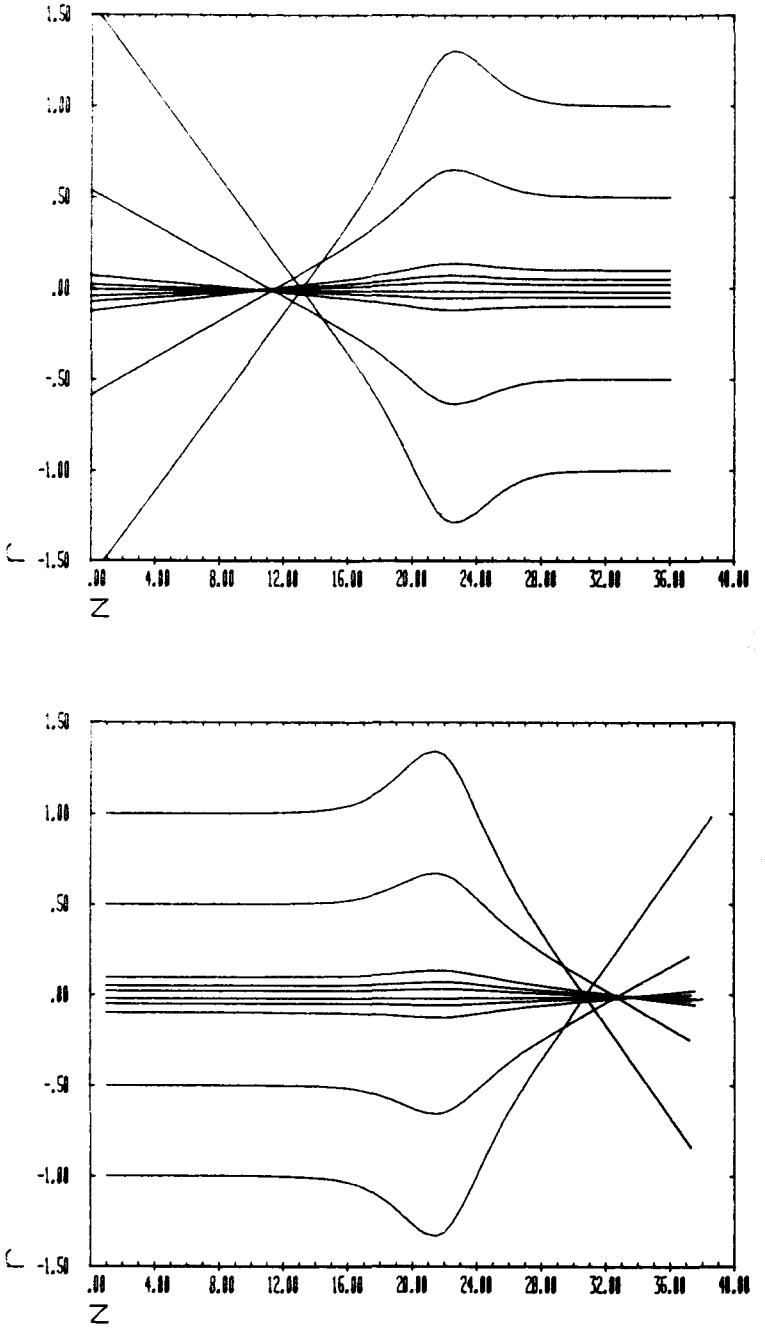

Fig. b.1.d *Idem.* $(V_2/V_1, V_3/V_1, V_4/V_1) = (1.0, 0.2, 1.0)$

$\frac{V_2}{V_1}$	$\frac{V_3}{V_1}$	$\frac{V_4}{V_1}$	non-paraxial $\mid r_o + 0.02$ mm $\mid = 0.5$ mm					paraxial				
			f_1 (H)	F_1 (H)	f_2 (H)	F_2 (H)	z_b (mm)	f_1 (H)	F_1 (H)	f_2 (H)	F_2 (H)	z_b (mm)
2.5	3.9	1.0	4.10	1.30	3.92	1.46	3.07	3.88	1.77	3.97	1.42	3.04
2.5	0.55	1.0	3.06	2.92	2.98	1.86	2.95	3.01	2.96	3.02	1.89	2.98
1.0	3.45	1.0	3.02	2.36	3.10	2.00	3.05	3.05	2.38	3.07	1.96	3.01
1.0	0.2	1.0	2.00	2.14	1.93	2.13	2.55	2.10	2.21	2.09	2.28	2.76

Table b.1 *Change in focal lengths and position vertical phase plane due to spherical aberration*